ELECTROCHEMICAL DEACTIVATION OF NITRATE, ARSENATE, AND TRICHLOROETHYLENE

BY

DHANANJAY MISHRA

A Dissertation Submitted to the Faculty of the

DEPARTMENT OF CHEMICAL AND ENVIRONMENTAL ENGINEERING

In Partial Fulfillment of the Requirements
For the Degree of

DOCTOR OF PHILOSOPHY
WITH A MAJOR IN ENVIRONMENTAL ENGINEERING

In the Graduate College

THE UNIVERSITY OF ARIZONA

2006

THE UNIVERSITY OF ARIZONA
GRADUATE COLLEGE

As members of the Dissertation Committee, we certify that we have read the dissertation prepared by Dhananjay Mishra

entitled Electrochemical Deactivation of Nitrate, Arsenate, and Trichloroethylene

and recommend that it be accepted as fulfilling the dissertation requirement for the Degree of Doctor of Philosophy

_____ Date: 7th August 2006
James Farrell

_____ Date: 7th August 2006
Wendell Ela

_____ Date: 7th August 2006
James Field

Final approval and acceptance of this dissertation is contingent upon the candidate's submission of the final copies of the dissertation to the Graduate College.

I hereby certify that I have read this dissertation prepared under my direction and recommend that it be accepted as fulfilling the dissertation requirement.

_____ Date: 7th August 2006
Dissertation Director: James Farrell

STATEMENT BY AUTHOR

This dissertation has been submitted in partial fulfillment of requirements for an advanced degree at the University of Arizona and is deposited in the University Library to be made available to borrowers under rules of the Library.

Brief quotations from this dissertation are allowable without special permission, provided that accurate acknowledgement of source is made. Requests for permission for extended quotation from or reproduction of this manuscript in whole or in part may be granted by the head of the major department or the Dean of the Graduate College when in his or her judgment the proposed use of the material is in the interests of scholarship. In all other instances, however, permission must be obtained from the author.

SIGNED: DHANANJAY MISHRA

ACKNOWLEDGEMENTS

I would first like to thank my advisor Dr. James Farrell. Jim has been my inspiration for the past four and a half years. I will remain grateful for his valuable guidance, concern, care, understanding and support throughout these years. I will benefit from the lessons that he taught and the attitude towards research that he has helped me to develop.

I would like to thank my mom and dad. Their continuous love and support kept me motivated and focused throughout my career. I would like to specially thank Rose Myers. Rose's continuous support and love made me feel at home away from home. I have great respect for her dedicated and unconditional support and love towards all the students. I would like to thank Arla, Joe, Eric, Judee and Lorenzo for their help.

I would also like to thank my colleagues Amlan, Desikan, Rohit, Mohammad, Kedar, Harpreet, Jainkang, Nianliu, Nikos, Kim, Susan, Carla, Umar, and Irail for their help throughout my stay at the University of Arizona. Ron LeBlanc has been a great help in developing my analytical and laboratory skills. I would like to thank Mike Kopplin from the College of Pharmacy for all the analyses and guidance that he provided.

Finally I want to thank all my friends: Kiran, Dinesh, Prasad, Nitin, Praveen, Milind, Sushant, Raj, Ashwini, Viral, Soni, Debashree, and Kartik.

TABLE OF CONTENTS

LIST OF FIGURES 7

LIST OF TABLES 10

ABSTRACT 11

CHAPTER 1 INTRODUCTION

1.1 Outline 14
1.2 Introduction 14

CHAPTER 2 UNDERSTANDING NITRATE REACTIONS WITH ZEROVALENT IRON USING TAFEL ANALYSIS AND ELECTROCHEMICAL IMPEDANCE SPECTROSCOPY

2.1 Abstract 16
2.2 Introduction 17
2.3 Materials and Methods 19
2.4 Results and Discussion 21
2.5 Acknowledgements 28
2.6 Figures 29

CHAPTER 3 EVALUATION OF MIXED VALENT IRON OXIDES AS REACTIVE ADSORBENT FOR ARSENIC REMOVAL

3.1 Abstract 38
3.2 Introduction 39
3.3 Materials and Methods 41
3.4 Results and Discussion 44
3.5 Reaction Product Analyses 52
3.6 Acknowledgements 53
3.7 Supporting Information 54
3.8 Figures 58

CHAPTER 4 UNDERSTANDING REDUCTIVE DECHLORINATION OF TRICHLOROETHENE ON BORON DIAMOND FILM ELECTRODE

4.1 Abstract 68
4.2 Introduction 68

TABLE OF CONTENTS—Continued

4.3 Electrochemical Kinetics 70
4.4 Materials and Methods 71
4.5 Results and Discussion 74
4.6 Competing Reactions 77
4.7 Acknowledgements 79
4.8 Figures 80

REFERENCES 86

LIST OF FIGURES

FIGURE 2.1: a) Nitrate and nitrite concentrations versus time in 240 mL reactors containing iron wires with WFO and AFO initial conditions. The surface area normalized zeroth order NO_3^- removal rate constants (k_0) were calculated from the slopes of the solid lines. b) Nitrate and nitrite concentrations versus time in 4.5 mL vials containing iron wires with WFO and AFO initial conditions..... 29

FIGURE 2.2: a) Tafel plots for an iron wire with an AFO initial condition in 1 mM NO_3^- solution as a function of elapsed time; b) Nyquist plot of the imaginary impedance (Z_{img}) versus the real impedance (Z_{real}) for the iron wire in part (a); c) Bode phase plots of the phase angle between the applied voltage and resulting currents as a function of the signal frequency for the iron wire in part (a); d) Corrosion currents versus elapsed time for the wire in part (a)……30

FIGURE 2.3: Nitrate concentrations versus time in 240 mL reactors containing iron wires with WFO and AFO initial conditions. At 18 days elapsed 3 mM $FeSO_4$ was added to both reactors. ……32

FIGURE 2.4: a) Tafel diagrams for an iron wire with a WFO initial condition in solutions with NO_3^- concentrations of 0, 1, 2, 4, 6, 8, 16, 32, 64 and 96 mM. Tafel scans were measured after equilibrating the wire for 24 hours with each solution. b) Corrosion currents as a function of the NO_3^- concentration for the Tafel scans in part (a); c) Bode phase plots associated with the iron wire in part (a). ……33

FIGURE 2.5: a) Tafel scans for an iron wire with a WFO initial condition in solutions with NO_2^- concentrations of 0, 0.1, 0.5, 1, 2, 4, 8, 16, 32 and 64 mM; b) Corrosion currents as a function of the NO_2^- concentration for the Tafel scans in part (a)……..35

FIGURE 2.6: Nitrite concentrations versus time in 240 mL reactors containing iron wires with WFO and AFO initial conditions. At 15 days elapsed 3 mM $FeSO_4$ was added to both reactors. ……36

FIGURE 3.1: a) Fraction of influent arsenic removed as a function of the As(V) feed concentration for an 8 min EBCT and 9 mg/L DO for media A (▲), B (●) and AC (□). The error bars on the data represent the range of three samples collected over several hundred empty bed volumes after achieving steady state effluent concentrations……58

LIST OF FIGURES --Continued

FIGURE 3.2: a) Batch measured media corrosion rates expressed in µmol·g-1·d-1 as a function of the dissolved oxygen concentration for media A (▲) and B (●) in the NaCl electrolyte and media C (□) in the tap water electrolyte……59

FIGURE 3.3: Arsenic removed as a function of the EBCT for media A (▲), B (●), and AC (□) for an As(V) feed concentration of 50 µg/L. Solid lines represent the fit of the pseudo-first order kinetic model to the data for media A (k=0.10 min-1), B (k=0.24 min-1) and AC (k=0.28 min-1); b) Molar ratio of Fe2+ released per As(V) removed for the data in part a. The rate of Fe2+ released is taken from Figure 2 at a DO concentration of 9mg/L…….60

FIGURE 3.4: Arsenic removed as a function of the dissolved oxygen concentration for a 50 µg/L As(V) feed concentration with at 8 min EBCT for media A (▲) and B (●) in the NaCl electrolyte, and media AC (□) in the tap water electrolyte…….....61

FIGURE 3.5: a) Arsenic removed as a function of the solution pH value for a 50 µg/L As(V) feed concentration with at 8 min EBCT for media A (▲) and B (●) in the NaCl electrolyte, and for media AC (□) in the tap water electrolyte; b) Corrosion currents as a function of the solution pH value measured with graphite paste electrodes for media A (▲) and B (●) in the NaCl electrolyte and media C (□) in the tap water electrolyte……62

FIGURE 3.6: S1) Comparison of the trends in corrosion rates measured using the batch (open symbols) and graphite paste electrode (solid symbols) methods for media A (▲, Δ) and B (●, ○) in the NaCl electrolyte and media C (■, □) in the tap water electrolyte…..63

FIGURE 3.7: S2) As(V) removal by columns of media A (▲) and B (●) in a $CaSO_4$ background electrolyte solution with varying silica concentrations for feed As (V) concentration of 50 µg/L ……..64

FIGURE 3.8: S3) a) Tafel scans for the media C graphite paste electrode in Tucson tap water containing no As(V) showing how the corrosion current (i_{corr}) is calculated from extrapolation of the linear regions of the cathodic and anodic scans; b) Tafel scans for the media C graphite paste electrode in Tucson tap water with As(V) concentrations ranging from 0 to 400 µg/L…….65

FIGURE 3.9: S4 Tafel scans for a graphite paste electrode composed of media A at DO concentrations of <0.01, 3 and 9 mg/L……..66

LIST OF FIGURES --Continued

FIGURE 4.1: a) Rate of TCE reduction (●)in µmol● hr^{-1} or current density (□) in mA●cm^{-2} on BDD surface at different electrode potential (V/SHE) for 7.5 mM TCE at 22 ^{0}C. …….80

FIGURE 4.2: a) TCE reduction rate in µmol● hr^{-1} vs inverse of reaction temperature (T^{-1}) at fixed TCE concentration of 3mM. b) Activation energies (kJ●mol^{-1}) as a function of electrode potential (V/SHE) calculated from part a……..…….81

FIGURE 4.3: a) Density functional theory simulation for the initial starting configuration for a diamond cluster with net charge of -1. b) Resulting chemisorbed complex for part a). ……..…82

FIGURE 4.4: Bode Phase plots of the phase angle between the applied voltage and resulting currents as a function of the signal frequency at 0 mM (□) and 7.5 mM (●)TCE concentration. ……..…..83

FIGURE 4.5: TCE reduction rate (□) in µmol● hr^{-1} on BDD surface as a function of the aqueous TCE concentration in mM at 22 ^{0}C and 15 mA●cm^{-2} and HAc (●) concentration (mM). ……84

FIGURE 4.6: a) Current efficiency (%) as a function of current density (mA●cm^{-2}) for 0.375mM (♦), 3mM (○), 7.5 mM (■) TCE on BDD surface and 3mM (*) TCE on iron surface. b) Surface area normalized rate constant k (cm/s) for part a). ……85

LIST OF TABLES

TABLE 2.1: Table shows the charge transfer resistance and corrosion potential for the graph in Figure 2-2 a……..……37

TABLE 3.1: Properties of the iron oxide media, iron corrosion products (Fe:As), and hydraulic conductivities of the packed columns, before and after use. Also listed are the changes in DO concentrations (ΔDO), solution pH values (ΔpH), and average effluent iron concentrations for the experiments depicted in Figure 1. The Darcy's law hydraulic conductivity (K) is defined in the supporting information…….…….. 67

ABSTRACT

This research investigated the mechanism, kinetics and feasibility of nitrate, arsenate, and trichloroethylene inactivation on zerovalent iron (ZVI), mixed-valent iron oxides, and boron doped diamond film electrode surfaces, respectively. Nitrate (NO_3^-) is a common co-contaminant at sites remediated using permeable reactive barriers (PRBs). Therefore, understanding nitrate reactions with ZVI is important for understanding the performance of PRBs. This study investigated the reaction mechanisms of NO_3^- with ZVI under conditions relevant to groundwater treatment. Tafel analysis and electrochemical impedance spectroscopy were used to probe the surface reactions. Batch experiments were used to study the reaction rate of NO_3^- with freely corroding and cathodically protected iron wires. Nitrate reduction was found to be a zeroth order process with respect to its aqueous concentration for both water formed oxide (WFO) and air formed oxide (AFO). Nitrate reaction with AFO and WFO resulted in stoichiometric production of nitrite and did not reach completion. This behavior was attributed to formation of a Fe(III) oxide that blocked access to Fe(II) on the ZVI surface which is necessary for sustaining the reactions. In case of AFO, a time lag was observed before nitrate removal commenced. The lag time was required for auto reduction of the Fe(III) layer present on air formed oxide surfaces. The presence of free Fe(II) in solution was found to enhance the rate of nitrate reactions on the ZVI surface. The removal kinetics for the AFO were 2.5 times slower than that of WFO. The faster removal in the case of the

WFO was due to presence of an Fe(II)/Fe(III) oxide that was readily available to react with aqueous nitrate.

This research also investigated the use of slowly corroding magnetite (Fe_3O_4) and wustite (FeO) as reactive adsorbent media for removing As(V) from potable water. Observed corrosion rates for mixed valent iron oxides were found to be 15 times slower than that of zerovalent iron under similar conditions. Electrochemical and batch and column experiments were performed to study the corrosion behavior and gain a deeper understanding on the effects of water chemistry and operating parameters, such as, empty bed contact times, influent arsenic concentrations, dissolved oxygen levels and solution pH values and other competing ions. Reaction products were analyzed by X-Ray diffraction and XPS to determine the fate of the arsenic. The reaction products formed from both media had Fe to As ratios of 15:1 in the absence of any competing ions. However, an Fe to As ratio of 150:1 was observed in Tucson water. The corrosion rates of both media were sufficiently slow to avoid column clogging over 90 days of operation. The planned use of the adsorbent media is in packed-bed filters in both large and small-scale treatment systems, as well as point of use filters suitable for an individual well-head or faucet. No regeneration of the adsorbent media is planned, and disposal of the spent media is expected to be as a non-toxic waste.

This research also investigated use of boron doped diamond film electrodes for reductive dechlorination of trichloroethylene (TCE). TCE reduction resulted in nearly stoichiometric production of acetate. Rates of TCE reduction were found to be independent of the electrode potential at potentials below -1 V with respect to the

standard hydrogen electrode (SHE). However, at smaller overpotentials, rates of TCE reduction were dependent on the electrode potential. Short lived species analysis and density functional simulations indicate that TCE reduction may occur by formation of a surface complex between TCE and carbonyl groups present on the surface.

CHAPTER 1

INTRODUCTION

1.1 Outline

This dissertation consists of five chapters. The first chapter describes the the motivation behind the research and gives an overview of current treatment technologies. Chapter 2 investigates nitrate reactions with zerovalent iron and has been published in the journal of *Environmental Science and Technology*. Chapter 3 investigates the usefulness of mixvalent iron oxide media for removing arsenate from potable water and has been published in the journal of *Environmental Science and Technology*. Chapter 4 investigates electrochemical reduction of trichloroethene on boron doped diamond (BDD) film electrodes.

1.2 Introduction

Nitrate, arsenate, and trichloroethylene are groundwater contaminants known to have adverse health effects on humans. The U.S. Environmental Protection Agency (USEPA) has imposed stringent drinking water standards for these contaminants. Available treatment technologies to remove these contaminants from ground water can be classified as phase transfer or destruction technologies.

Phase transfer technologies transfer contaminants from water to either an adsorbent or concentrate them in a brine stream. Phase transfer unit operations do not destroy target compounds. Adsorption on granular activated carbon, air stripping, reverse osmosis, filtration, coagulation and sedimentation technologies are classic examples of

phase transfer treatment technologies. Concentrated contaminants from these unit operations need to be treated before disposing into landfill.

In contrast, contaminant destruction technologies break target compounds into environmental friendly byproducts which are known to have less or no adverse health effects. Advanced oxidation and reduction, UV light, thermal treatment, and electrochemical assisted oxidation and reduction technologies are classic examples of destructive treatment technologies.

Research presented in this dissertation focuses on destruction technologies for nitrate and TCE, and a phase transfer technology for arsenate.

CHAPTER 2

UNDERSTANDING NITRATE REACTIONS WITH ZEROVALENT IRON USING TAFEL AND ELECTROCHEMICAL IMPEDANCE SPECTROSCOPY

2.1 Abstract

This study investigated the reaction mechanisms of nitrate (NO_3^-) with zerovalent iron ZVI media under conditions relevant to groundwater treatment using permeable reactive barriers (PRB). Reaction rates of NO_3^- with freely corroding, or cathodically and anodically polarized, iron wires were measured in batch reactors. Tafel analysis and electrochemical impedance spectroscopy (EIS) were used to investigate the reactions occurring on the iron surfaces. Reduction of NO_3^- by corroding iron resulted in near stoichiometric production of NO_2^-, which did not react in the absence of added *Fe(II)*. Increasing NO_3^- concentrations resulted in increasing corrosion currents. However, EIS and Tafel analyses indicated that there was little direct reduction of NO_3^- at the ZVI surface. This behavior can be attributed to NO_3^- induced formation of a microporous oxide on the iron surfaces that blocked NO_3^- and NO_2^- reduction, but not water reduction. Nitrite concentrations greater than 4 mM resulted in anodic passivation of the iron, but NO_3^- concentrations up to 96 mM did not result anodically controlled corrosion. This indicates that the passivating oxide preventing NO_3^- reduction was permeable towards cation migration. The main mechanism for both NO_3^- and NO_2^- reduction was reaction with *Fe(II)*-containing oxides coating the iron surface. This indicates that short-term batch tests requiring little turnover of reactive sites on the iron surface may over estimate

long-term rates of NO_3^- removal because the effects of passivation are not apparent in batch tests conducted with high initial *Fe(II)* to NO_3^- ratios. The ability of nitrate to promote the formation of a microporous oxide is consistent with previous observation that NO_3^- impedes reduction of trichloroethylene by ZVI.

2.2 Introduction

Permeable reactive barriers containing zerovalent iron (ZVI) are being increasingly utilized for in situ remediation of groundwater contaminated by chlorinated solvents, regulated metals, and radionuclides (*1-5*). The ZVI serves as a reducing agent for reductive dechlorination of solvents and reductive precipitation of redox active metals. Corrosion of ZVI produces *Fe(II)*-containing oxides, such as ferrous hydroxide, magnetite (*6*), and green rusts (*7*), that may also serve as reducing agents. Iron oxides containing only *Fe(III)*, such as maghemite ($\gamma - Fe_2O_3$) and lepidocrocite ($\gamma - FeOOH$), may also remove contaminants via both physical and chemical adsorption (*8*).

Nitrate (NO_3^-) is one of the main co-contaminants found at sites containing solvent, metal, or radionuclide contamination (*9*). However, its reaction mechanisms with ZVI are poorly understood. The range of products produced from NO_3^- reduction by ZVI media suggests that there are several reaction mechanisms. Some studies have reported that NO_3^- may be fully reduced to ammonia (NH_3) (*10-16*), while other studies have reported incomplete NO_3^- reduction to nitrite (NO_2^-) and nitrogen (N_2) (11,*17*,*18*). These different products suggest that small changes in the reaction conditions may have a significant impact on the reaction mechanisms.

In addition to affecting the terminal reaction products, the reaction conditions also affect the reaction kinetics. For example, several investigators have reported that NO_3^- reduction by ZVI was first order in nitrate concentration (12,13), while other investigators have reported reaction rates that were zeroth order in NO_3^- concentration (14). The reaction order may also change over time, and several investigators have reported increasing deviations from first order kinetics with time (12,*19*), while other investigators have found that NO_3^- reduction ceased completely after a period of reaction (16,19-*21*).

In addition to passivation of the ZVI towards NO_3^- reduction, several studies have reported that NO_3^- passivates ZVI for reduction of chlorinated solvents (16,21,*22*). For example, one study reported that trichloroethylene (TCE) dechlorination rates in 3 mM NO_3^- solutions were a factor of three slower than those in chloride or sulfate electrolytes of the same ionic strength (16). Other studies have reported that reduction of TCE by ZVI completely stopped after exposure to 1.62 mM nitrate (21). This behavior was attributed to formation of a passivating layer of lepidocrocite on the iron surfaces. The profound effect of NO_3^- on TCE dechlorination rates makes understanding its reactions with ZVI essential for designing PRBs, and for determining appropriate conditions for their use.

This research investigated the reaction mechanisms of NO_3^- with ZVI media. Towards that end, reaction rates of NO_3^- with iron wires were determined. Additionally,

electrochemical experiments were performed to determine the effect of NO_3^- on iron corrosion rates and on the impedance to charge transfer at the iron surfaces.

2.3 Materials and Methods

Experiments measuring rates of NO_3^- removal were performed using two different iron surface areas to solution volume ratios. Experiments with a surface area density ($a_{\square}$ of 0.042 cm^2/mL were conducted in 240 mL cells using three 9 cm long by 0.12 cm diameter iron wires. Iron wires of 99.9% purity obtained from Aesar (Ward Hill, MA) and Sigma (St. Louis, MO) were used as received, and were suspended through septa in the lids of the reaction cells. The cells were continuously purged with 50 mL/min of nitrogen gas in order to exclude oxygen and mildly agitate the solutions. Experiments with an $a_{\square}$ value of 1.34 cm^2/mL were conducted in 4.5 mL sealed vials using four 4 cm long by 0.12 cm diameter iron wires. The reported $a_{\square}$ values are based on the nominal surface area of the wires, and were considerably lower than those normally used under field conditions and in other laboratory investigations. The low $a_{\square}$ values were used to minimize adsorption as a removal mechanism, and to require multiple turnover of reactive sites on the iron surface in order to effect measurable amounts of NO_3^- removal.

Removal rate experiments with freely corroding iron wires were performed in 3 mM $CaSO_4$ background electrolyte solutions with initial pH values of 7. Reactant concentrations were controlled by adding $NaNO_3$ of 99.26% purity or $NaNO_2$ of 97% purity to the background electrolyte solutions. In experiments investigating NO_3^- removal by iron coated with a water-formed oxide (WFO), the $NaNO_3$ was added to the

solutions after equilibrating the wire for 24 hours with the $CaSO_4$ background electrolyte. In experiments investigating NO_3^- removal by iron coated with an air-formed oxide (AFO), the wires were inserted into solutions containing NO_3^- at the desired concentration.

Concentrations of NO_3^- and NO_2^- were determined via ion chromatography using a Dionex (Sunnyvale, CA) model DX500 ion chromatograph with a detection limit of ~10 µg/L. Concentrations of NH_3 and NH_4^+ were measured via spectrophotometry using the phenate method (*23*) with a detection limit of 50 µg/L. Solution pH values were determined using pH test paper calibrated in increments of 1 pH unit.

All electrochemical experiments were performed in 850 mL glass cells containing a 10 cm long wire as working electrode, a stainless steel counter electrode, and a calomel reference electrode. The solutions were continuously purged with humidified nitrogen gas at the rate of 50 mL/min. Electrochemical experiments were performed using an EG&G (Oak Ridge, TN) model 273A scanning potentiostat and EG&G Powersuite software. All potentials are reported with respect to the standard hydrogen electrode (SHE).

Tafel analyses were performed to assess the effect of NO_3^- and NO_2^- on the cathodic and anodic reactions. Tafel diagrams were produced by polarizing each iron wire ±200 mV with respect to its open circuit potential at a scan rate of 5 mV/s (*24*). Experiments investigating the effect of anodically generated *Fe(II)* were performed using an iron wire cathode at a fixed potential of -600 mV, and iron or stainless steel wires as the anode. In order to minimize polarization effects on NO_3^- concentrations at the anode and cathode

surfaces, the fixed potential experiments were performed at a higher ionic strength in a solution consisting of 100 mM $NaCl$.

Electrochemical impedance spectroscopy (EIS) experiments were performed to determine the charge transfer resistance and the number of reactions occurring on the iron surfaces. The EIS measurements were made by applying a sinusoidal waveform with an amplitude of ±10 mV over a frequency range from $5x10^{-3}$ to 10^4 Hz. These experiments were performed by coupling the potentiostat with an EG&G model 5210 impedance phase analyzer. EG&G ZsimpWin software was used to fit the impedance data to a modified Randles circuit where the capacitor was replaced by a constant phase element in order to account for surface roughness and heterogeneities (*25*,*26*).

2.4 Results and Discussion

Nitrate and nitrite concentrations in batch reactors with an $a_{\square}$ value of 0.042 cm^2/mL containing iron wires with two different initial conditions are shown in 2-1a. For both the AFO and WFO initial conditions, there was a small amount of NO_3^- removal followed by a period in which there was no measurable removal. Solution pH values remained within 1 pH unit of neutral pH over the course of the experiments. The NO_2^- concentrations in each reactor increased as NO_3^- was removed, and then leveled off as NO_3^- reduction ceased. The nitrogen mass balance indicated near stoichiometric reduction of NO_3^- to NO_2^-. Absorption spectroscopy analyses did not show any detectable levels of NH_3 or NH_4^+, indicating that production of these species accounted for less than 3% of the total NO_3^- removed. Because NO_2^- is known to be a much stronger oxidant

than NO_3^- (24), the absence of any measurable NO_2^- reduction indicates that NO_3^- passivated the iron with respect to NO_2^- reduction.

Nitrate and nitrite concentrations in repeat experiments in reactors with an $a_{\square}$ value of 1.34 cm^2/mL are shown in Figure 2.1b. Results from these experiments were similar to those observed in Figure 1.1a, except that measurable NO_3^- reduction ceased at an earlier elapsed time, and after slightly less NO_3^- removal. For both the AFO and WFO initial conditions, the nitrogen mass balance indicated near stoichiometric production of NO_2^-, and detectable levels of NH_3 or NH_4^+ were not observed.

Polarization experiments were used to gain insight into the reaction behavior exhibited in Figure 2.1. Figure 2.2a shows Tafel scans and Figure 2.2b shows Nyquist plots at different elapsed times for an iron wire with an AFO initial condition in electrolyte solutions with an initial NO_3^- concentration of 1 mM. Table 2.1 summarizes the free corrosion potentials (E_{corr}) and charge transfer resistances (R_{ct}) determined from the plots in Figures 2.2a and 2.2b. Ten minutes after immersion of the wire into the NO_3^- solution, the E_{corr} value was -280 mV, as shown by the data in Figure 2.2a for 10 min elapsed. However, after 6 hours elapsed the E_{corr} value for the wire decreased to -510 mV. This decrease in potential was accompanied by an increase in the charge transfer resistance from 1020 to 3610 □. Since rates of cathodic reactions increase with decreasing potential, the increase in R_{ct} concomitant with the decrease in potential between 10 minutes and 6 hours elapsed is indicative of depletion of the reducible species responsible for the low R_{ct} at 10 minutes elapsed. This behavior can be attributed to

autoreduction of *Fe(III)* in the AFO after immersion into solution. The ionic conductivity provided by the solution allowed the underlying zerovalent metal to decrease the *Fe(III)/Fe(II)* ratio from levels consistent with an AFO, to levels that were closer to equilibrium with anaerobic water. Thus, the increasing R_{ct} values between 10 min and 6 hours elapsed arose from decreasing *Fe(III)* concentrations in the oxide layer. The fact that autoreduction of the oxide occurred in NO_3^- solutions indicates that NO_3^- itself was not sufficiently oxidizing to enforce a passivating *Fe(III)* layer, as in the case of other passivators, such as chromate (29).

The Bode phase plots in Figure 2.2c indicate that water reduction was the primary cathodic reaction after 6 hours elapsed. Each peak in the profiles corresponds to a reaction that affects the impedance to current flow (*27*). At ten minutes elapsed the Bode plot shows two peaks. The peak centered near 0.003 Hz corresponds to *Fe(III)* reduction, and the peak centered near 0.3 Hz corresponds to the Volmer proton discharge reaction, which is known to be the rate-limiting step for hydrogen evolution under these conditions (*28*). For times between 6 hours and 9 days elapsed, there was only 1 peak in each profile. This peak corresponds to that for proton discharge. The presence of only 1 cathodic reaction indicates that direct NO_3^- reduction did not significantly contribute to the corrosion current.

The cathodic Tafel slopes (β_c) and the corrosion currents between 6 hours and 9 days elapsed also indicate that water reduction was the primary cathodic reaction after 6 hours elapsed. The β_c values for the data taken between 6 hours and 9 days elapsed ranged from 0.0059 to 0.0070 dec/mV. These β_c values are close to the range of 0.0060

to 0.0072 dec/mV previously observed for water reduction at iron surfaces in neutral pH solutions (*29-32*). As shown in Figure 2.2d, the corrosion currents (I_{corr}) remained nearly constant between 6 hours and 9 days elapsed, despite cessation of NO_3^- reduction by 8 days elapsed. This suggests that the NO_3^- reduction taking place during the first 8 days elapsed did not involve direct oxidation of the ZVI. Nitrate reduction via reaction with *Fe(II)* released at anodic sites is consistent with this behavior, since this reaction would not directly influence the Tafel slope, the corrosion current, or the EIS profiles.

The effect of anodically generated *Fe(II)* on rates of NO_3^- removal was investigated in fixed potential experiments using iron wire cathodes and stainless steel or iron wire anodes. The primary anodic reaction on the iron anode was *Fe(II)* generation, while oxygen evolution was the anodic reaction on the stainless steel anode. At a cathode potential of -600 mV, the experiment using the iron anode had a NO_3^- removal rate of 890 μmol/cm^2/day, which was 2.1 times the rate observed with the stainless steel anode. Because the iron cathodes in both experiments were held at the same potential, the difference in NO_3^- removal rates can be attributed to reaction with anodically generated *Fe(II)*.

The importance of *Fe(II)* to reduction of NO_3^- by freely corroding iron was investigated by adding 3 mM $FeSO_4$ to batch reactors containing iron wires with AFO and WFO initial conditions. Figure 2.3 shows the NO_3^- concentrations as a function of time in two reactors. As previously observed, NO_3^- removal decreased below measurable levels by 8 days elapsed. However, after addition of $FeSO_4$ at 17 days elapsed, rapid

nitrate reduction to NH_4^+ was observed. In experiments where $FeSO_4$ was added to homogeneous solutions containing 1 mM NO_3^-, rates of nitrate removal were more than two orders of magnitude slower than those observed in Figure 2.3. This indicates that *Fe(II)* oxides coating ZVI are much more reactive towards NO_3^- reduction than dissolved *Fe(II)* species. This behavior is consistent with previous observations with other oxidants that *Fe(II)* adsorbed to *Fe(III)* oxides is a stronger reducing agent than aqueous *Fe(II)* (*33*).

Although NO_3^- passivated the iron with respect to its own reduction, it did not passivate the iron towards water reduction. Figure 2.4a shows Tafel scans obtained in solutions with NO_3^- concentrations ranging from 0 to 96 mM. Increasing NO_3^- concentrations produced monotonic increases in I_{corr}, as shown in Figure 2.4b. However, NO_3^- reduction was not responsible for most of the increase in I_{corr}. For the data in Figure 2.4a, the increase in I_{corr} after addition of 1 mM NO_3^- to the blank electrolyte was a factor of 4.5 greater than the NO_3^- removal rate, on an electron equivalent basis. Furthermore, the single peak in all Bode plots in Figure 2.4c shows that there was only one reaction that had a significant impact on the impedance, even for NO_3^- concentrations as high as 96 mM. The similar cathodic Tafel slopes in the blank and NO_3^- solutions is also consistent with hydrogen evolution as the primary cathodic reaction for all NO_3^- concentrations.

The ability of NO_3^- to increase the iron corrosion rate in the absence of significant NO_3^- reduction can be attributed to nitrate's effect on the oxide coating the iron surfaces.

In the absence of nitrate or other strong oxidants, iron in anaerobic solutions becomes coated with a layer of Fe_3O_4 (29). The open circuit potential in the blank solution of -550 mV is consistent with the equilibrium potential between *Fe* and Fe_3O_4 at neutral pH values (*34*). However, past investigators have reported that NO_3^- reactions with iron result in formation of lepidocrocite, $\gamma - FeOOH$ (21). Lepidocrocite is formed by rapid oxidation of $Fe(OH)_2$ under neutral pH conditions, while magnetite is formed via slow oxidation of ferrous hydroxides (*35*). The fact that lepidocrocite is microporous (35) may allow water reduction, but not NO_3^- reduction due to size exclusion. The increase in the corrosion current in the presence of NO_3^- may be attributed to the greater porosity of a lepidocrocite coating as compared to a magnetite coating. Additionally, part of the increase in the corrosion current may have resulted from acidity generated by oxidizing Fe_3O_4 to $\gamma - FeOOH$ as shown by:

$$Fe_3O_4 + 2H_2O \rightarrow 3FeOOH + H^+ + e^- \quad (1)$$

The mechanism by which NO_3^- passivates ZVI contrasts with the passivation mechanism induced by other common contaminants. For example, high halocarbon and CrO_4^{2-} concentrations were found decrease ZVI reactivity via an anodic passivation mechanism in which an *Fe(III)* oxide prevented release of *Fe(II)* into the solution at anodic sites (16, 29). In contrast, the Tafel scans in Figure 2.4a show that NO_3^- had only a minor effect on the anodic reactions, even at concentrations as high as 96 mM. This indicates that the *Fe(III)* oxide produced from NO_3^- reduction was sufficiently porous to allow *Fe(II)* diffusion to the solution interface.

Although high NO_3^- concentrations did not result in anodically controlled corrosion, NO_2^- concentrations above 4 mM resulted in anodic inhibition of iron corrosion, as illustrated by the Tafel scans in Figure 2.5a and the corrosion currents in Figure 2.5b. Increasing NO_2^- concentrations between 0 and 4 mM resulted in higher corrosion currents. However, increasing NO_2^- concentrations above 4 mm resulted in decreasing corrosion currents. For NO_2^- concentrations between 0 and 4 mM, the increase in I_{corr}, despite decreasing anodic currents indicates that iron corrosion was cathodically controlled, with water reduction as the primary corrosion limiting reaction. However, for NO_2^- concentrations above 4 mM, the sharp decrease in the anodic currents was sufficient to make the overall corrosion process limited by the rate of *Fe(II)* generation. The net result is that the overall corrosion currents decreased with increasing NO_2^- concentrations above 4 mM. The fact that NO_2^- resulted in anodic inhibition of iron corrosion can be attributed to it being a much stronger oxidant than NO_3^- (34).

Although NO_2^- is a stronger oxidant than NO_3^-, it rapidly passivates corroding iron media towards its own reduction. Figure 2.6 shows NO_2^- concentrations in batch reactors with an $a_{\square}$ value of 0.042 cm^2/mL containing iron wires with two different initial conditions. For both the WFO and AFO initial condition, there was no measurable NO_2^- removal over a 16 day period. However, addition of 3 mM $FeSO_4$ resulted in rapid NO_2^- reduction to NH_4^+. Similarly as with NO_3^-, the iron wire was required to promote rapid NO_2^- reduction. In homogeneous solutions containing 6 mM $FeSO_4$, NO_2^- removal rates were 20 times slower than those in Figure 2.6.

Results from this study help explain the wide range of results obtained by previous investigators of NO_3^- reduction by ZVI media. The incomplete reduction products observed here may be attributed to the extent of reactive site turnover required to affect measurable amounts of NO_3^- removal. Past studies showing more complete NO_3^- reduction have been carried out with $a_{\square}$ values ranging from 47 to 9000 times greater than those used in this investigation (12,19). More complete NO_3^- reduction may also be observed in batch studies where the reaction vials are agitated for mixing purposes. Particle-particle contact during mixing may result in abrasion of oxides from the iron surfaces, and may thereby prevent formation of the passive coating that stops NO_3^- reduction. Thus, some batch studies of NO_3^- reduction by ZVI media may not mimic the reaction conditions in a real PRB. In addition to the aforementioned differences between short-term batch tests and field conditions, microbiological activity may impact the effect of NO_3^- on the reactivity of ZVI media (9).

2.5 Acknowledgements

This project was made possible by grant number 2P42ES04940-11 from the National Institute of Environmental Health Sciences of the National Institute of Health, with funds from the U.S. Environmental Protection Agency.

2.6 Figures

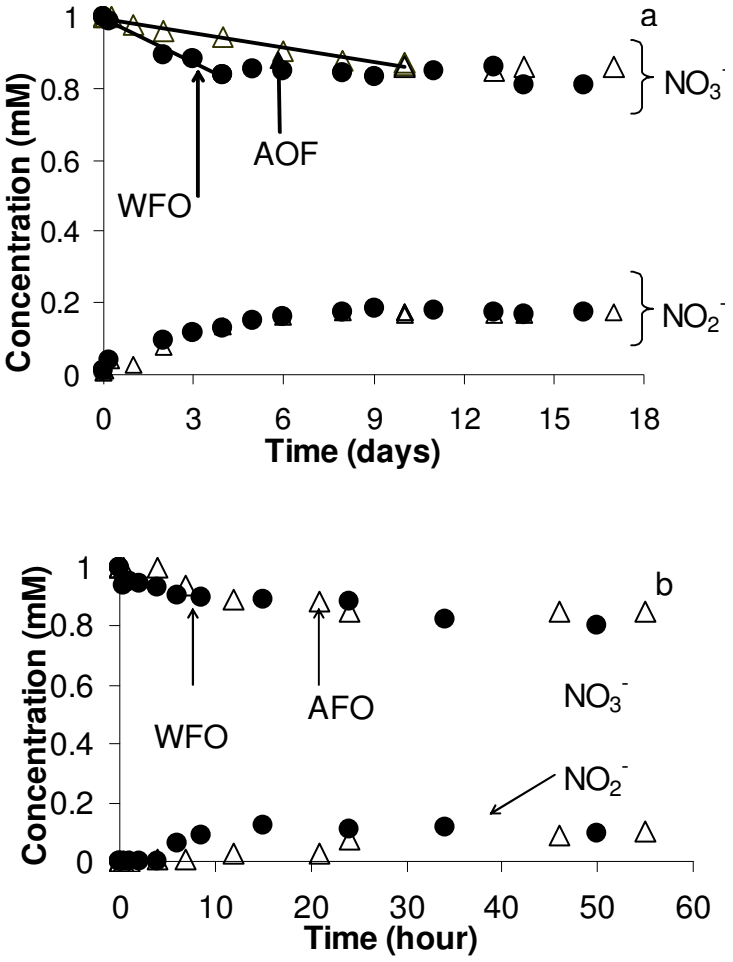

Figure 2.1: a) Nitrate and nitrite concentrations versus time in 240 mL reactors containing iron wires with WFO and AFO initial conditions. The surface area normalized zeroth order NO_3^- removal rate constants (k_0) were calculated from the slopes of the solid lines. b) Nitrate and nitrite concentrations versus time in 4.5 mL vials containing iron wires with WFO and AFO initial conditions.

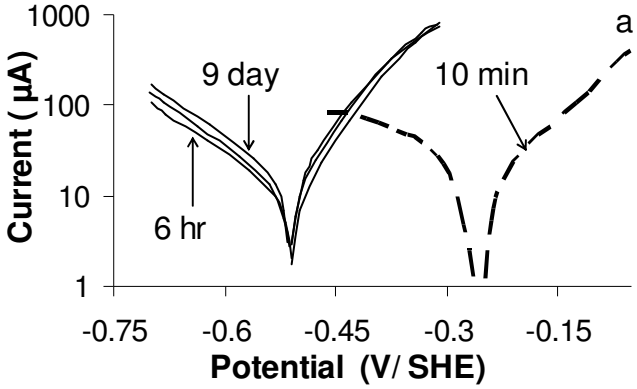
a
1000
100
10
1
Current (µA)
9 day
10 min
6 hr
-0.75
-0.6
-0.45
-0.3
-0.15
Potential (V/ SHE)

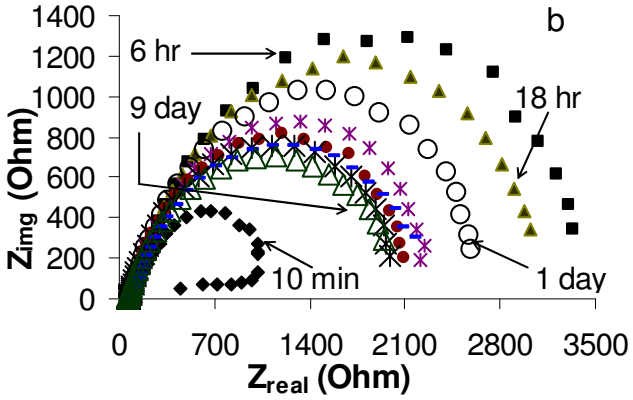
b
1400
1200
1000
800
600
400
200
0
Zimg (Ohm)
6 hr
9 day
18 hr
10 min
1 day
0
700
1400
2100
2800
3500
Zreal (Ohm)

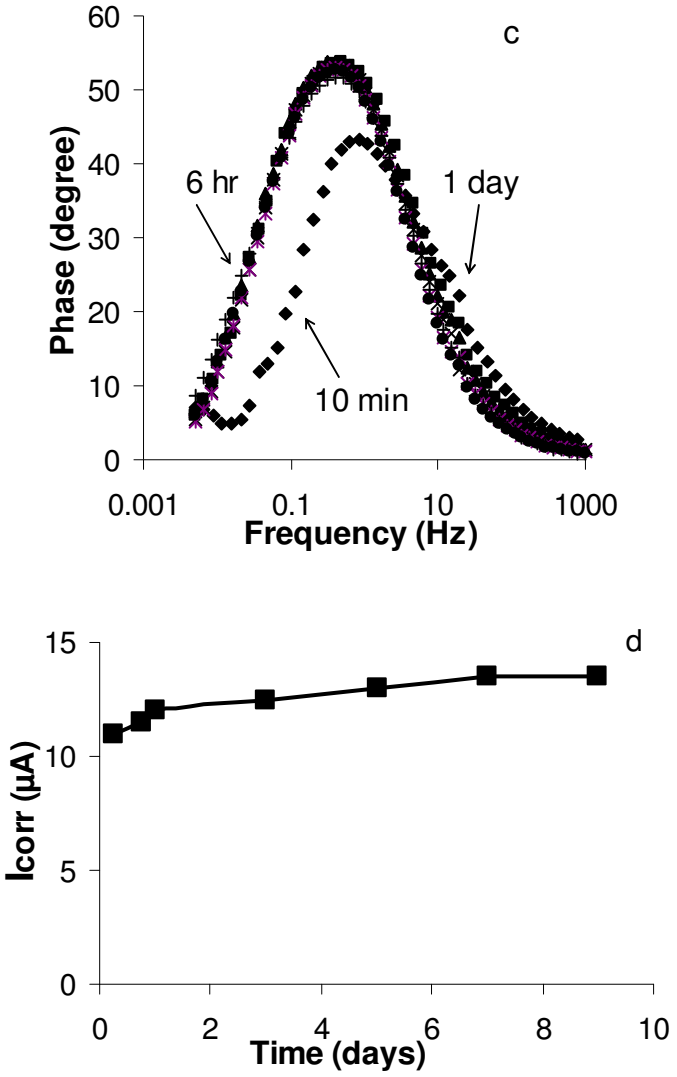

Figure 2.2: a) Tafel plots for an iron wire with an AFO initial condition in 1 mM NO_3^- solution as a function of elapsed time; b) Nyquist plot of the imaginary impedance (Z_{img}) versus the real impedance (Z_{real}) for the iron wire in part (a); c) Bode phase plots of the phase angle between the applied voltage and resulting currents as a function of the signal frequency for the iron wire in part (a); d) Corrosion currents versus elapsed time for the wire in part (a).

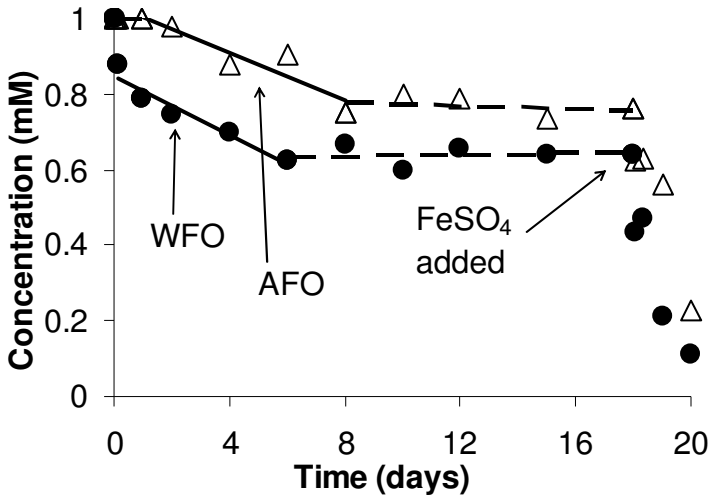

Figure 2.3: Nitrate concentrations versus time in 240 mL reactors containing iron wires with WFO and AFO initial conditions. At 18 days elapsed 3 mM $FeSO_4$ was added to both reactors.

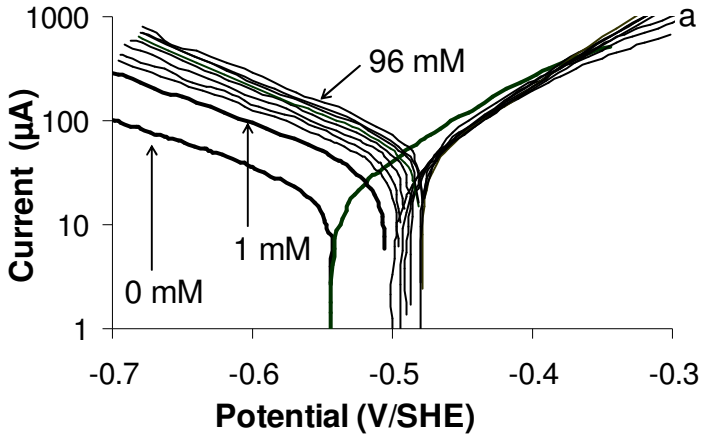
1000
100
10
1
Current (µA)
96 mM
1 mM
0 mM
a
-0.7
-0.6
-0.5
-0.4
-0.3
Potential (V/SHE)

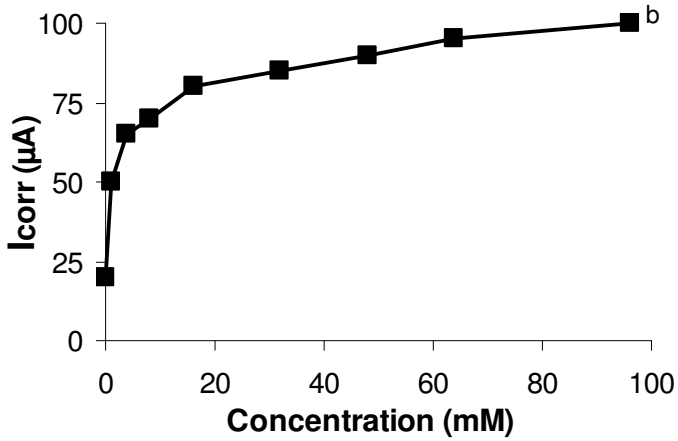
100
75
50
25
0
Icorr (µA)
b
0
20
40
60
80
100
Concentration (mM)

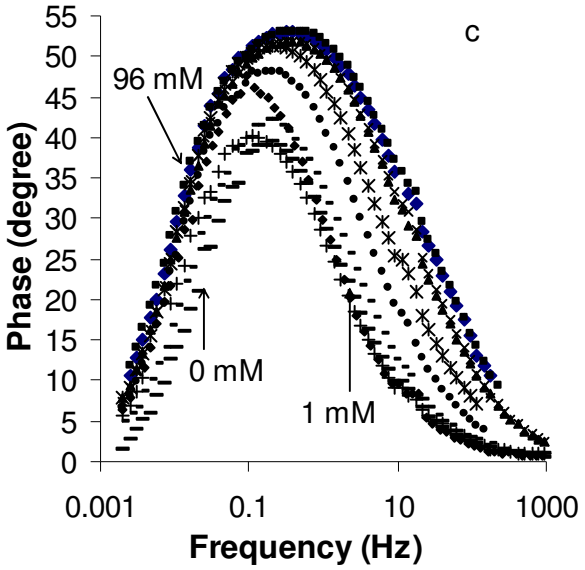

Figure 2.4: a) Tafel diagrams for an iron wire with a WFO initial condition in solutions with NO_3^- concentrations of 0, 1, 2, 4, 6, 8, 16, 32, 64 and 96 mM. Tafel scans were measured after equilibrating the wire for 24 hours with each solution. b) Corrosion currents as a function of the NO_3^- concentration for the Tafel scans in part (a); c) Bode phase plots associated with the iron wire in part (a).

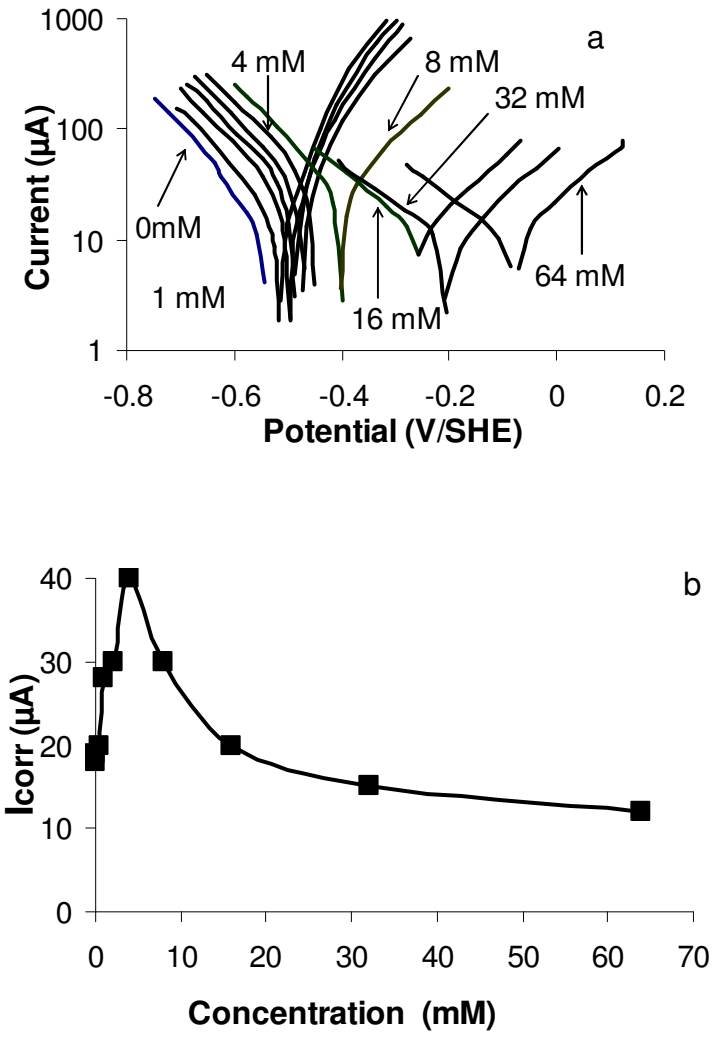

Figure 2.5: a)Tafel scans for an iron wire with a WFO initial condition in solutions with NO_2^- concentrations of 0, 0.1, 0.5, 1, 2, 4, 8, 16, 32 and 64 mM; b) Corrosion currents as a function of the NO_2^- concentration for the Tafel scans in part (a).

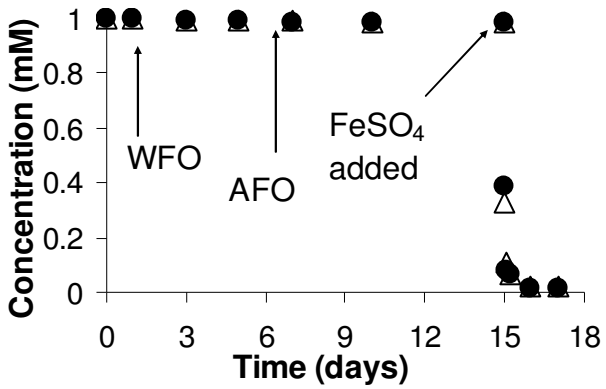

Figure 2.6: Nitrite concentrations versus time in 240 mL reactors containing iron wires with WFO and AFO initial conditions. At 15 days elapsed 3 mM $FeSO_4$ was added to both reactors.

Table 2.1: Table shows the charge transfer resistance and corrosion potential for the graph in Figure 2-2 a.

Time (days)	Charge transfer resistance (Rct, Ω)	Corrosion potential (Ecorr, V)
10 min	1020	-0.280
6 hr	3610	-0.510
18 hr	3230	-0.510
1	2760	-0.510
2	2360	-0.510
4	2190	-0.510
6	2175	-0.510
9	2050	-0.510

CHAPTER 3

EVALUATION OF MIXED VALENT IRON OXIDES AS REACTIVE ADSORBENT FOR ARSENIC REMOVAL

3.1 Abstract

The objective of this research was to determine if Fe(II)-bearing iron oxides generate ferric hydroxides at sufficient rates for removing low levels of arsenic in packed bed reactors, while at the same time avoiding excessive oxide production that contributes to bed clogging in oxygenated waters. Column experiments were performed to determine the effectiveness of three media for arsenic removal over a range in empty bed contact times, influent arsenic concentrations, dissolved oxygen (DO) levels, and solution pH values. Corrosion rates of the media as a function of the water composition were determined using batch and electrochemical methods. Rates of arsenic removal were first order in the As(V) concentration and were greater for media with higher corrosion rates. As(V) removal increased with increasing DO levels primarily due to faster oxidation of the Fe^{2+} released by media corrosion. In order to obtain measurable amounts of arsenic removal in 15 mM NaCl electrolyte solutions containing 50 µg/L As(V), the rate of Fe^{2+} released by the media needed to be at least 15 times greater than the As(V) feed rate into the column. In waters containing 30 mg/L of silica and 50 µg/L As(V), measurable amounts of arsenic removal were only obtained for Fe^{2+} release rates that were at least 200 times greater than the As(V) feed rate. Although all columns showed losses in hydraulic conductivity over the course of 90 days of operation, the conductivity values remained high, and the losses could be reversed by backwashing the media. The reaction

products produced by the media in domestic tap water had average As to Fe ratios that were ~25% higher than those for a commercially available adsorbent.

3.2 Introduction

Iron oxides (*36-45*) and zerovalent iron (ZVI) filings (*46-50*) have been found to be effective at removing arsenic compounds from water. Granular iron oxides in the form of poorly crystalline akaganeite (*51*) or goethite (*52*) are commonly used to remove arsenic by public utilities in packed-bed adsorption systems. Zerovalent iron filings have been added to household filters for arsenic removal in developing nations (*53-55*), and have also been used in permeable reactive barriers for intercepting arsenic plumes in contaminated groundwater (*56*). The primary arsenic removal mechanism for both granular iron oxides and ZVI filings involves the formation of mono- and bi-dentate complexes between arsenic species and ferric hydroxides (37, 40, 43, *57*).

Although granular ferric hydroxides are effective adsorbents for arsenic removal, there are several problems associated with their use. High arsenic adsorption capacities require high adsorbent porosity, which results in granules that are very friable and easily compacted. Compaction of the media requires frequent backwashing in order to maintain the hydraulic conductivity in packed bed adsorbers (*58*). Granular ferric hydroxides also suffer from slow adsorption kinetics. Although complex formation between arsenic species and ferric hydroxides is extremely rapid (41), arsenic removal is usually limited by intragranular diffusion to available adsorption sites (*59*). Diffusion of arsenic species into ferric hydroxide grains is very slow, with effective intragranular diffusion coefficients ranging from 5 to 7 orders of magnitude smaller than diffusion coefficients

for the arsenic species in bulk solution (*60*). Recent evidence indicates that more than 18 days may be required to reach adsorption equilibrium for granular adsorbents with particle diameters greater than 0.25 mm (60). The high diffusional mass transfer resistance for arsenic adsorption often leads to early breakthrough, and the bed must be retired before a significant fraction of its capacity can be utilized (58).

In oxygenated waters there are also problems associated with the use of ZVI filings for arsenic removal. Corrosion of ZVI results in the release of Fe^{2+} at anodic sites. Oxidation of Fe^{2+} by dissolved oxygen (DO) followed by cation hydrolysis then produces ferric hydroxides which serve as sites for adsorption of both As(V) and As(III) compounds (47, 48, *57*, *61*). The major problem with ZVI media for arsenic removal in waters containing several mg/L of DO is that its rate of corrosion is much greater than needed for generating sufficient adsorption sites for the low concentrations of arsenic that are typically found in drinking water supplies. Once formed, the oxides begin aging and lose surface area and porosity with time, and contribute to mass transfer limitations for arsenic removal. The fast corrosion rates of ZVI media in oxygenated waters also results in high concentrations of dissolved iron in the treated water. A recent study using packed columns of ZVI filings reported effluent iron concentrations ranging from 0.3 to 20 mg/L (49).

The problems resulting from the high corrosion rates of ZVI in oxygenated waters suggest that iron containing media with slower corrosion rates may be useful for arsenic removal in waters containing several mg/L of DO. Corrosion of Fe(II)-bearing oxides in oxygenated waters has the advantage of continuously generating high surface area ferric

hydroxides, but avoids the excessive oxide generation associated with ZVI. This may result in greater amounts of As(V) removed per Fe^{2+} released.

The main goal of this research was to determine if the corrosion rates of Fe(II)-bearing iron oxide media are sufficiently fast for removing practical amounts of As(V) from water, but not too fast to result in column clogging and mass transfer limitations for arsenic removal. Three mixed valent iron oxides were screened for their ability to remove arsenate from water, and for their propensity to generate iron oxides that contribute to bed clogging. Column experiments were performed to determine the effect of hydraulic detention time, influent As(V) concentration, solution pH value, and DO concentration on arsenate removal by each media. The effects of these parameters on media corrosion rates were also determined in order to elucidate the mechanisms controlling arsenic removal.

3.3 Materials and Methods

Arsenate removal was studied using the three iron oxide media listed in Table 3.1. The compositions of the media were selected to span a range in reactivity towards oxidation by dissolved oxygen. The media are produced from metal recycling operations and are commercially sold as pigments and abrasives. Properties of the media were supplied by the manufacturer, PEL Technologies (Canton, OH). The media were produced in large monoliths and were crushed and sieved to obtain the particle size ranges shown in Table 3.1. Powder X-ray diffraction (XRD) and X-ray photoelectron spectroscopy (XPS) were used to characterize the media and their reaction products with

As(V) after use. The XRD and XPS analyses were performed by the Arizona Materials Laboratory at the University of Arizona.

Arsenic removal experiments were performed in 1.5 cm internal diameter by 45 cm long ACE Glass (Vineland, NJ) chromatography columns with packed bed depths of 10 cm. Columns were packed with either 55 g of media A, 50 g of media B or a mixture of 55 g media A and 55 g media C. It was necessary to dilute media C with media A because preliminary tests found that columns packed with 100% media C suffered from flow channeling due to cementation of neighboring granules by corrosion products. Falling head permeameter tests (*62*) were used to determine the Darcy's law hydraulic conductivities (K) (*63*) of the packed columns before and after use. Properties of the packed columns are shown in Table 3.1.

Experiments were performed in dechlorinated Tucson tap water and in 15 mM NaCl background electrolyte solutions spiked with As(V). The columns were operated with influent As(V) concentrations ranging from 50 to 800 µg/L prepared by adding $Na_2HAsO_4 \bullet 7H_2O$ (Sigma, St. Louis, MO) of 99.8% purity to the electrolyte solutions. Solution pH values were adjusted by adding small amounts of concentrated NaOH or HCl (Sigma), and were determined using pH test strips (EM Sciences, Gibbstown, NJ) calibrated in increments of 0.3 pH units. The columns were operated with empty bed contact times (EBCTs) ranging from 1 to 16 minutes and with DO concentrations ranging from <0.01 to 9 mg/L. Oxygen concentrations in the feed solutions were controlled using a counter-current water-gas contactor purged with mixtures of ultra high purity oxygen and nitrogen. Dissolved oxygen concentrations in the influent and effluent solutions

were determined in a sealed, glass, flow-through cell using an Extech Instruments (Waltham, MA) oxygen electrode with a detection limit of 0.01 mg/L.

Concentrations of arsenic and iron were determined via inductively coupled plasma mass spectrometry (ICP-MS) using EPA method 6020A (*64*) and an Agilent model 7500a ICP-MS. The minimum reporting level for both arsenic and iron species was 1 µg/L. Effluent arsenic and iron concentrations for each set of operating conditions were obtained by taking three samples over a period of several hundred empty bed volumes after achieving steady state effluent concentrations. The error bars on the data represent the range of the three samples. Dissolved silica concentrations were determined colorimetrically to a precision of ±0.5 mg/L (as SiO_2) using EPA method 0370.1 (*65*) with Hanna (El Paso, TX) test kits.

The corrosion behavior of the iron oxide media as a function of the solution pH value, DO and As(V) concentrations were determined using both batch and electrochemical methods. The batch tests involved placing 2 g of each media in a small flask containing 25 mL of the background electrolyte solution with no added As(V). The sealed flasks were purged for one week with mixtures of ultra pure oxygen and nitrogen corresponding to DO concentrations of <0.01, 3 and 9 mg/L. After one week, the supernatant of the solutions were decanted and the media were extracted 3 times with an oxalic acid solution in order to dissolve the ferric corrosion products (39, *66*). The amount of iron in the supernatant and extracts were then determined using ICP-MS. Iron concentrations in the third extraction were less than 2% of those in the first extraction. This indicates that 2 extractions were able to remove nearly all the ferric corrosion

products, and that the oxalic acid solutions did not corrode the media to an experimentally significant extent.

Tafel analyses using graphite paste electrodes were performed to determine how the solution chemistry affected the corrosion rate of each media. The working electrodes were constructed by pressing finely ground samples of each media into wet, conductive, graphite epoxy coated on the end of a 0.5 cm diameter graphite rod. The graphite was electrically insulated from the solution by placing the rod inside a heat-shrink Teflon sleeve. The electrochemical experiments were conducted in an 850-mL glass cell containing a platinum wire counter electrode and a saturated calomel reference electrode. The electrode cell was continuously purged with humidified nitrogen and oxygen gas mixtures at a rate of 50 mL/min. Potentials were controlled and currents were recorded using an EG&G (Oak Ridge, TN) model 273A scanning potentiostat and EG&G Powersuite software. Tafel diagrams were produced by polarizing each graphite paste electrode ± 200 mV with respect to its open circuit potential at a scan rate of 5 mV/s. The correlation between the corrosion rates determined in the batch experiments and those determined using the graphite paste electrodes are illustrated in the supporting information in Figure 3.6.

3.4 Results and Discussion

The column operating conditions used in this study were selected to investigate the arsenic removal effectiveness of the three media under conditions that are relevant to drinking water treatment, and also under conditions that will probe the rate limiting

mechanisms and removal limitations of each media. The EBCTs used in this study were similar to those commonly used in packed bed adsorption systems for arsenic removal (49, 51, 58), and the influent As(V) concentrations spanned a similar range as those reported for drinking water supplies. Although municipal water supplies in the United States typically use source waters containing less than 50 µg/L of arsenic, concentrations as high as 800 µg/L have been reported in water supplies in developing nations (*67*). The two different background electrolytes were selected to span a range in As(V) removal difficulty. Experiments were performed in the NaCl electrolyte in order to understand the behavior of the media in the absence of other anions that may interfere with As(V) removal. Experiments were performed in Tucson tap water because it contains high concentrations of silica, which is known to compete with As(V) for adsorption sites on iron oxide media (*68- 72*).

The effect of the feed concentration on As(V) removal by all three media was investigated by varying the influent concentration between 50 and 800 µg/L at a pH value of 6.5 and an influent DO concentration of 9 mg/L. Figure 3.1 shows the fraction of the influent As(V) that was removed by each media as a function of the feed concentration for a flow rate of 2.25 mL/min. This flow rate corresponds to an EBCT of 8 min for columns containing media A and B, and 16 min for columns containing media AC. The data for media A and B were generated in the 15 mM NaCl background electrolyte, while the data for media AC was obtained in Tucson tap water. Effluent iron concentrations and the changes in DO and solution pH values between the influent and effluent ends of each column are shown in Table 3.1. The small changes in DO levels and pH values

indicate that these parameters were nearly constant along the length of each column. The effluent iron concentrations were all below the secondary drinking water standard of 300 µg/L, and were 2 to 3 orders of magnitude lower than those reported for columns containing 100% ZVI filings (49).

In a different set of experiments (not shown in figure), media A and B were not effective for removing practical amounts of arsenic in Tucson tap water, while media AC removed 100% of the influent As(V) under all conditions in the NaCl electrolyte. Columns of media A and B operated using 50 µg/L As(V) in tap water with an EBCT of 8 minutes showed average As(V) removals of less than 2% over the course of 80 days of operation. However, both these media were effective for arsenic removal in the NaCl electrolyte, as shown by the data in Figure 3.1. The poor performance of media A and B in the tap water can be attributed to the high concentration of silica (30 mg/L) which competed with As(V) for adsorption sites. Figure 3.7 in the supporting information shows that for media A and B at As (V) feed concentration of 50 µg/L, there is a near linear decline in As(V) removal with increasing silica concentration, and there is <2% As(V) removal at a silica concentration of 400 µg/L.

The decreasing fractional removal with increasing As(V) feed concentration shown in Figure 3.1 is consistent with a mechanism where arsenic removal is limited by the availability of adsorption sites generated by media corrosion. Tafel scans with the graphite paste electrodes showed that the corrosion rates of all three media were not measurably affected by the As(V) concentration, as illustrated by Figure 3.8 in the supplemental information. At a DO level of 9 mg/L, the batch corrosion data in Figure 3-

2 indicate that the corrosion rates of media B and C were 4 and 70 times, respectively, greater than that for media A. Therefore, the better removal performance of media B versus A in the NaCl electrolyte is consistent with a removal rate that is limited by the rate of adsorption site generation resulting from media corrosion.

For media AC the decrease in the fractional As(V) removal was not monotonic with increasing feed concentration. This behavior can be explained by competition for adsorption sites between As(V) and silica species. Silica concentrations in the influent tap water were 30±0.5 mg/L, and in the effluent water were 26-27 ±0.5 mg/L for an As(V) feed concentration of 50 µg/L. Increasing As(V) feed concentrations resulted in decreasing amounts of silica removed. For an As(V) feed concentration of 800 µg/L, the amount of silica removed was 0.5±0.5 mg/L. Between feed concentrations of 50 and 800 µg/L the amount of As(V) removed increased by 4.9 µmol/L (365 µg/L) while at the same time the amount of silica removed decreased by 50 µmol/L (3 mg/L). Displacement of ~10 SiO_2 species by adsorption of one As(V) species may be attributable to electrostatic interactions between adsorbed species and/or to desorption of oligomeric silica species (*73*).

The effect of EBCT on arsenic removal was investigated by varying the flow rate for a 50 µg/L influent As(V) solution with a pH value of 6.5 and a DO concentration of 9 mg/L. Figure 3.3a shows the amount of As(V) removed as a function of the EBCT for the A and B media in 15 mM NaCl, and for the AC media in Tucson tap water. Figure 3.3b shows the moles of iron released per mole of arsenic removed (Fe:As) in each column based on the corrosion rate data in Figure 3.2 and the removal data in Figure

3.3a. The Fe:As ratios in the reaction products shown in Table 3.1 are consistent with those shown in Figure 3.3b, confirming that the corrosion behavior in the columns was similar to that in the batch tests. The arsenic removal data in Figure 3.3a can be described by a pseudo first order kinetic model of the form:

$$\frac{d[\text{As(V)}]}{dt} = -\text{k}\ [\text{As(V)}] \qquad (1)$$

where [As(V)] is the aqueous arsenate concentration and k is a rate constant. The fit of the kinetic model to the As(V) removal data is illustrated by the solid lines in Figure 3.3a. For the two columns operated in the NaCl electrolyte, the rate constants differ by a factor of 2.4 while their respective corrosion rates at a DO level of 9 mg/L differ by a factor of 4. This shows that there is less than a proportional increase in the rate constant with increasing corrosion rate. Media specific factors, such as, surface charge or surface area, that may impact adsorption of Fe^{2+} or the nucleation of ferric hydroxide precipitates, may contribute to the nonlinear relationship between k and the media corrosion rate.

Although removal rates that are pseudo first order in the As(V) concentration are consistent with surface mediated reactions that are limited by hydrodynamic boundary layer mass transfer, mass transfer limitations on As(V) removal were small under all operating conditions. For a 16 min EBCT, the mass transfer correlation of Wilson and Geankoplis (*74*) for a packed bed of spherical particles (non porous) yields a boundary layer mass transfer rate constant of 42 min^{-1} for media A and AC, and 65 min^{-1} for media B. These mass transfer rate constants are more than two orders of magnitude greater than the removal rate constants determined for each media. At shorter EBCT values the boundary layer mass transfer rate constants are even larger.

The effect of DO on rates of As(V) removal and media corrosion are shown in Figure 3.4 for a 50 µg/L As(V) feed concentration at a pH value of 6.5. For all three media, the amount of As(V) removed increased with increasing DO concentration. This behavior can be attributed to the effects of oxygen on rates of Fe^{2+} generation and subsequent oxidation to Fe(III). Rate constants reported for oxidation of dissolved Fe^{2+} indicate that the oxidation half-life at a DO concentration of 0.01 mg/L is 79 min, but is only 0.36 min at a DO concentration of 9 mg/L (*75*). As shown in Figure 3.2, the corrosion rate of media A decreased with increasing DO levels between <0.01 and 9 mg/L. Associated with this decrease in corrosion current was an 18 µg/L increase in the amount of As(V) removed. This behavior indicates that at low DO levels, rates of As(V) removal by media A were controlled by rates of Fe^{2+} oxidation and not by the rate of Fe^{2+} generation via media corrosion. As shown in Figure 3.9 in the supporting information, the decreasing corrosion rate with increasing DO for media A can be attributed to the ability of oxygen to enforce a passivating film at anodic sites on the media. For media B and AC, the increases in corrosion rate with increasing DO levels were always smaller than the increases in As(V) removal. For example, between DO levels of <0.01 and 3 mg/L, there was a 25% increase in the corrosion rate of media B, and a 600% increase in As(V) removal. The greater impact of DO on the As(V) removal versus the corrosion rate shows that the rate of Fe^{2+} oxidation was the primary factor affecting As(V) removal at DO levels below 3 mg/L. At a DO concentration of 9 mg/L, the Fe^{2+} oxidation half-life of 0.36 min suggests that the rate of Fe^{2+} oxidation was not a rate limiting factor for As(V) removal. The corrosion rate data in Figure 3.2 along with the measured effluent

iron concentrations indicate that >99% of the media corrosion products remained in the columns at all DO levels. Therefore, the low As(V) removals at DO levels <0.01 mg/L indicate that the corrosion products formed in nearly anoxic waters are not effective for adsorbing arsenic.

The effect of the influent solution pH value on As(V) removal is shown in Figure 3.5a for an 8 min EBCT with a feed solution containing 50 µg/L As(V) and 9 mg/L DO. In all cases, effluent pH values were not measurably different than influent values. As(V) removal by media B and AC decreased when the solution pH was increased from 5 to 8. This decrease in removal can partly be attributed to 42 and 45% decreases in corrosion rates for media B and AC, respectively. For media B, there was a larger decrease in As(V) removal (60%) as compared to the corrosion rate (42%) between pH values of 5 and 8. This is consistent with previous observations of decreased As(V) binding to ferric hydroxides with increasing pH values (*76*). For media AC, the complete As(V) removal at pH values of 5 and 6.5 make it impossible to determine if the decrease in As(V) removal was greater than the decrease in corrosion rate. For media A, there were no statistically significant changes in the corrosion rate or As(V) removal between pH values of 5 and 8.

The performance of media A and B remained stable over the course of the investigation. For an EBCT of 8 minutes and a 50 µg/L As(V) feed concentration, arsenic removal over the first several days of steady state operation was 55±3% by media A and 90±4% by media B. After 90 days of operation, As(V) removal by media A and B were 51±3% and 86±4%, respectively. This shows that the media was able to maintain

its reactivity for over 16,000 empty bed volumes. A second column of media B (results not shown) run with an EBCT of 20 minutes showed ~100% As(V) removal for over 50 days, at which time the experiment was terminated. The nearly constant performance of media A and B can be attributed to the fact that only a small fraction of each media corroded during the course of the investigation. Based on the corrosion rate data in Figure 3.2 at a DO concentration of 9 mg/L, less than 0.2% of media A and <0.6% of media B corroded over the course of 90 days.

The reactivity of columns packed with media AC showed a sharp loss in arsenic removal after 60 days elapsed. The amount of As(V) removed by a column packed with media AC that was operated under constant conditions with an influent concentration of 50 µg/L and an EBCT of 4 minutes declined from 25 µg/L to 3 µg/L between 60 and 90 days elapsed. During this declining period of As(V) removal, the effluent iron concentrations declined from 40 to 7 µg/L. This decline in performance can likely be attributed to exhaustion of the Fe(0) fraction of media C. Assuming that the measured corrosion rate of 20 µmol/(g-d) for media C was all due to Fe(0), the metallic iron in media C would last 46 days. Therefore, the declining performance of media C after 60 days elapsed is consistent with corrosion rate data. Additionally, XRD and XPS analyses of media C measured after 90 days elapsed did not show the presence of any Fe(0) in the spent media.

The hydraulic conductivity (K) of all columns declined over the course of the investigation, as shown in Table 3.1. However, the hydraulic conductivity of all three columns remained greater than that for coarse sand, which has a hydraulic conductivity of

~0.1 cm/s (63). Backwashing the columns at a flow rate of 100 mL/min was able to restore most of the losses in hydraulic conductivity as shown by the post-backwash data in Table 3.1.

3.5 Reaction Product Analyses

Reaction products taken from each column were analyzed by XRD and XPS, and the Fe:As ratios were determined by acid digestion followed by ICP-MS analysis. For all three columns no crystalline products could be identified. The absence of crystalline reaction products is consistent with past findings that poorly crystalline ferric hydroxides are produced from reactions of iron corrosion products with As(V) (47, 57), and that iron hydroxide precipitates containing more than 1-3% As(V) do not crystallize (*77*, *78*). The Fe:As ratios in the reaction products from each column are shown in Table 3.1. For media A and B, the Fe:As ratios are smaller than the value of 70:1 measured on a commercial adsorbent (Bayoxide E33®, AdEdge Technologies) in the same electrolyte at an As(V) feed concentration of 50 µg/L. For column AC the reaction products had an Fe:As ratio of 380:1, and the value for a second column of media AC run at a constant influent As(V) concentration of 50 µg/L was 400:1. These Fe:As ratios are only ~25% smaller than the Fe:As ratio of 520:1 obtained for the commercial media in Tucson tap water at an As(V) concentration of 50 µg/L. This indicates that in real waters the reactive adsorbent media does not achieve substantially greater As(V) loadings than preformed granular ferric hydroxides.

This study indicates that mixed valent iron media with corrosion rates several orders of magnitude slower than that of zerovalent iron can remove practical amounts of As(V) from water only when high concentrations of competing adsorbates are absent. In waters without competitively adsorbing species, practical levels of As(V) removal required that the rate of Fe^{2+} generation by media corrosion was at least 15 times greater than the As(V) feed rate into the column, as shown by the data in Figure 3.3b for media A. In waters containing 30 mg/L of silica, practical levels of As(V) removal occurred only when the rate of Fe^{2+} generation was more than two orders of magnitude greater than the feed rate of As(V), as shown by the data in Figure 3.3b for media AC. Although the two media without any Fe(0) content corroded too slowly for use in packed bed adsorption systems, their corrosion rates may be sufficiently high for use in permeable barrier remedial systems which operate at EBCT values on the order of 1 day or more.

3.6 Acknowledgements

This project was made possible by grant number 2P42ES04940-11 from the National Institute of Environmental Health Sciences of the National Institutes of Health, with funds from the U.S. Environmental Protection Agency. The authors thank Mike Kopplin, Phil Anderson and Ken Nebesny for analytical support and Abid Bengali, Robert Wolfe, and Jeff Cheatham at PEL Technologies for materials and financial support.

3.7 Supporting Information

Comparison of Batch Electrode Corrosion Measurements:

The effect of the solution pH value, As(V) and DO concentrations on the media corrosion rates were determined using graphite paste electrodes. This procedure was necessary because it was not possible to vary only one parameter at a time in the batch corrosion experiments. Corrosion currents measured with the graphite paste electrodes were used to determine only the trend in corrosion rates of each media as one parameter was varied. The absolute values of the corrosion currents measured for each media cannot be compared since the surface areas of the crushed media on the paste electrodes were not representative of the surface areas of the native granules. Figure 3.6 compares the corrosion rate trends for each media with varying DO level measured using the batch and graphite paste electrode methods. For each media there was a close correlation between the change in current and the change in Fe^{2+} generation rate accompanying a change in DO level. The greatest disparity between the two methods was for media C between DO levels of <0.01 and 3 mg/L. This can be attributed to the fact that the batch tests likely underestimated the corrosion rate of media C at a DO level of <0.01 mg/L. Media C contained 5.3% Fe(0). Corrosion of Fe(0) in anaerobic water produces magnetite (*79*), which is not extracted by the oxalic acid solution.

Effect of Silica on As(V) Removal by Media A and B:

Two hypotheses were tested to determine why the performance media A and B was superior in the NaCl versus tap water electrolyte. Chloride ions are well-known to enhance iron corrosion rates (79). To determine if 15 mM Cl^- was responsible for enhancing media performance, experiments were performed in a $CaSO_4$ background electrolyte with an ionic strength of 15 mM. The Tucson tap water used in this study contained ~30 mg/L of dissolved silica. To determine if silica in the tap water competed with As(V) for adsorption sites, experiments were performed with varying concentrations of silica added to the $CaSO_4$ electrolyte. Figure 3.7 shows the amount of As(V) removed by media A and B as a function of the silica concentration in the $CaSO_4$ electrolyte. At a silica concentration of 0 µg/L, the performance of both media was similar to that in the NaCl electrolyte. However, increasing silica concentrations decreased As(V) removal by each media until there was less than 2% removal at a silica concentration of 400 µg/L. This behavior indicates that silica competes with As(V) for adsorption sites generated by the media. Given that the silica concentration in the tap water was a factor of 75 times greater than that needed to inhibit measurable amounts of As(V) removal in the $CaSO_4$ electrolyte, the poor performance of media A and B in tap water can be attributed to the competitive adsorption of silica.

Effect of the As(V) Concentration on Media Corrosion Rates:

Tafel scans performed with the graphite paste electrodes indicated that the As(V) concentration did not have a measurable effect on the corrosion rates of the media. As illustrated in Figure 3.8 for media C, increasing the As(V) concentration from 0 to 400

µg/L had no measurable effect on the cathodic scans, but did have a small effect on the anodic scans. However, within the precision of the graphical technique, the point of intersection of the extrapolated Tafel slopes (which yields the corrosion current, i_{corr}) were not measurably affected by the As(V) concentration. Similar results were obtained for media A and B.

Effect of the DO Concentration on Corrosion of Media A:

The decreasing corrosion rates with increasing DO concentrations that were observed for media A in the batch corrosion experiments can be attributed to increasing anodic inhibition with increasing DO concentration. When the overall rate of media oxidation does not depend on the concentration or chemical nature of the oxidant (*i.e.*, the cathodic depolarizing species), the corrosion rate is anodically controlled. For Fe(II)-bearing oxides, anodically controlled corrosion is limited by the rate at which Fe^{2+} can be released into the solution. Release of Fe^{2+} at anodic sites may be limited by intracrystalline diffusion of Fe^{2+}, or by a surface film that prevents the Fe^{2+} released at anodic sites from entering the solution (79). The Tafel scans in Figure 3.9 indicate that increasing DO levels resulted in an increasingly passivating anodic film. Comparison of the cathodic Tafel scans at DO concentrations of <0.01, 3, and 9 mg/L shows that higher cathodic currents were obtained at higher DO concentrations. Additionally, the cathodic Tafel slope changed between <0.01 and 3 mg/L DO. This can be attributed to a change in the cathodic reaction from water reduction to O_2 reduction. Comparison of the anodic Tafel scans shows that increasing DO concentrations resulted in decreasing anodic currents. Because the overall corrosion rate followed the downward trend in anodic

currents (rather than the upward trend in cathodic currents) with increasing DO, corrosion of the media is therefore anodically controlled.

Darcy's Law:

The hydraulic conductivity is defined by Darcy's law as (*80*):

$$Q = KA\frac{dH}{dx} \tag{1}$$

where Q is the volumetric flow rate (cm^3/s), K is the hydraulic conductivity (cm/s), A is the cross sectional area normal to the direction of water flow (cm^2), and dH(cm)/dx(cm) is the head loss per unit distance.

3.8 Figures

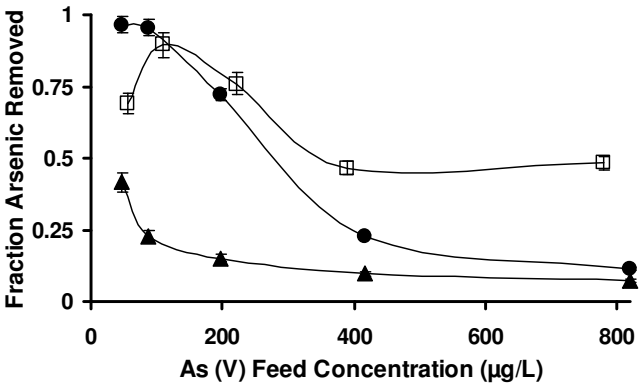

Figure 3.1: a)Fraction of influent arsenic removed as a function of the As(V) feed concentration for an 8 min EBCT and 9 mg/L DO for media A (▲), B (●) and AC (□). The error bars on the data represent the range of three samples collected over several hundred empty bed volumes after achieving steady state effluent concentrations.

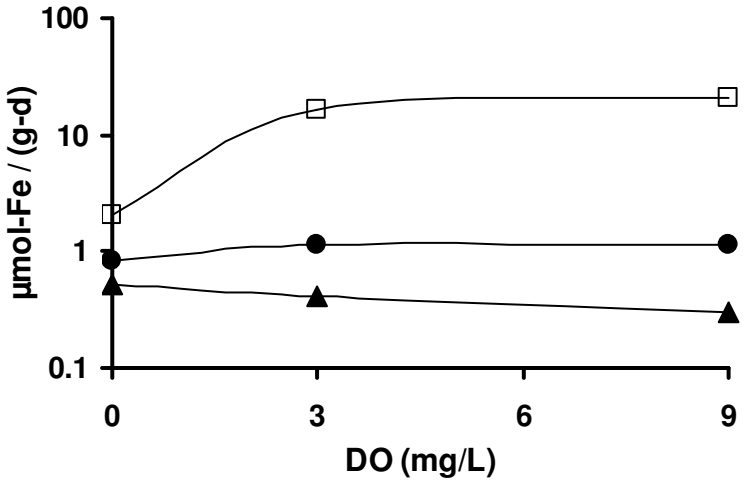

Figure 3.2: a) Batch measured media corrosion rates expressed in µmol·g-1·d-1 as a function of the dissolved oxygen concentration for media A (▲) and B (●) in the NaCl electrolyte and media C (□) in the tap water electrolyte.

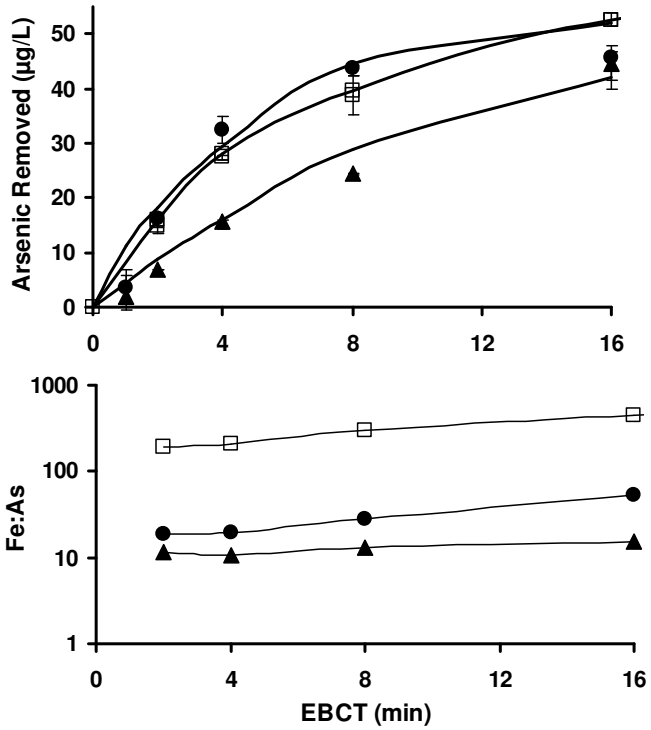

Figure 3.3: Arsenic removed as a function of the EBCT for media A (▲), B (●), and AC (□) for an As(V) feed concentration of 50 µg/L. Solid lines represent the fit of the pseudo-first order kinetic model to the data for media A (k=0.10 min-1), B (k=0.24 min-1) and AC (k=0.28 min-1); b) Molar ratio of Fe2+ released per As(V) removed for the data in part a. The rate of Fe2+ released is taken from Figure 3.2 at a DO concentration of 9 mg/L.

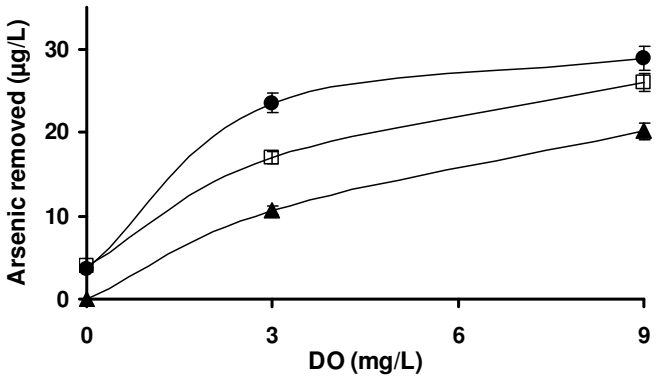

Figure 3.4: Arsenic removed as a function of the dissolved oxygen concentration for a 50 µg/L As(V) feed concentration with at 8 min EBCT for media A (▲) and B (●) in the NaCl electrolyte, and media AC (□) in the tap water electrolyte.

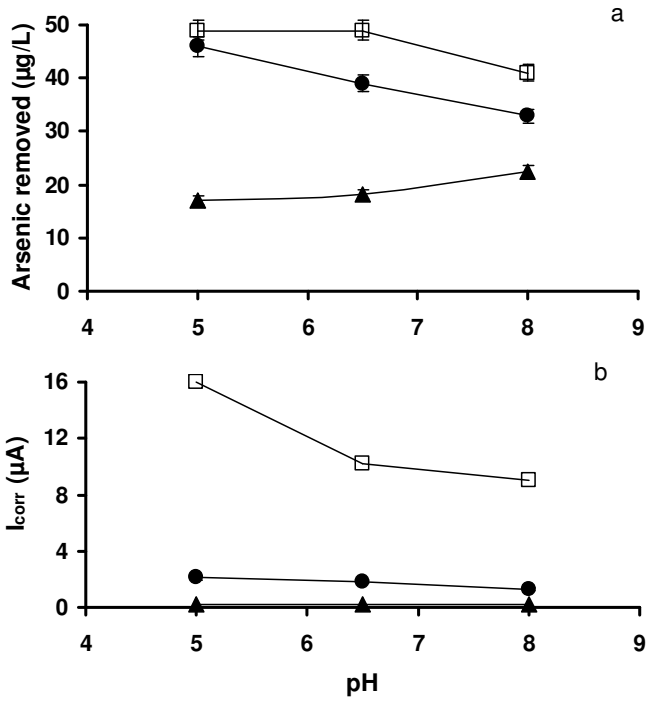

Figure 3.5: a) Arsenic removed as a function of the solution pH value for a 50 µg/L As(V) feed concentration with at 8 min EBCT for media A (▲) and B (●) in the NaCl electrolyte, and for media AC (□) in the tap water electrolyte; b) Corrosion currents as a function of the solution pH value measured with graphite paste electrodes for media A (▲) and B (●) in the NaCl electrolyte and media C (□) in the tap water electrolyte.

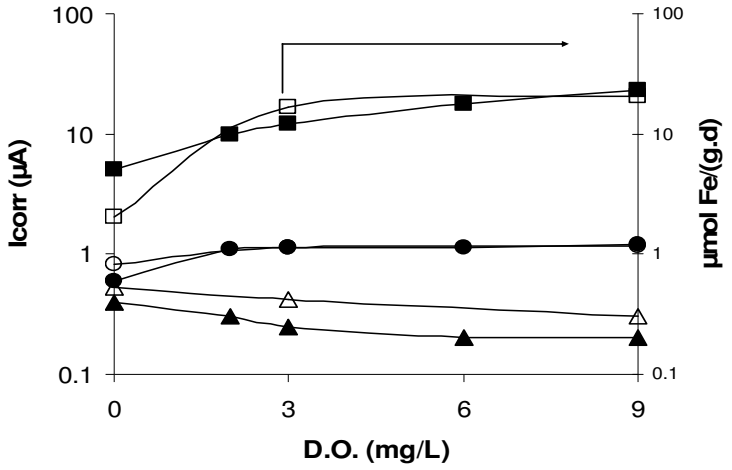

Figure 3.6: Comparison of the trends in corrosion rates measured using the batch (open symbols) and graphite paste electrode (solid symbols) methods for media A (▲, Δ) and B (●, ○) in the NaCl electrolyte and media C (■, □) in the tap water electrolyte.

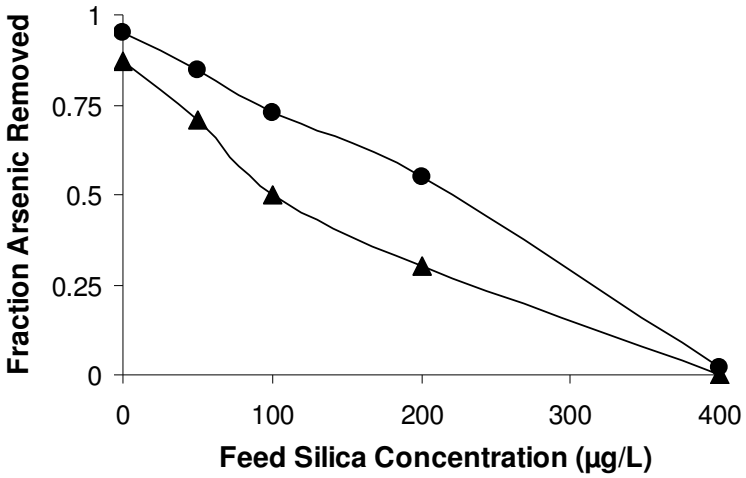

Figure 3.7: As(V) removal by columns of media A (▲) and B (●) in a $CaSO_4$ background electrolyte solution with varying silica concentrations for feed As (V) concentration of 50 µg/L.

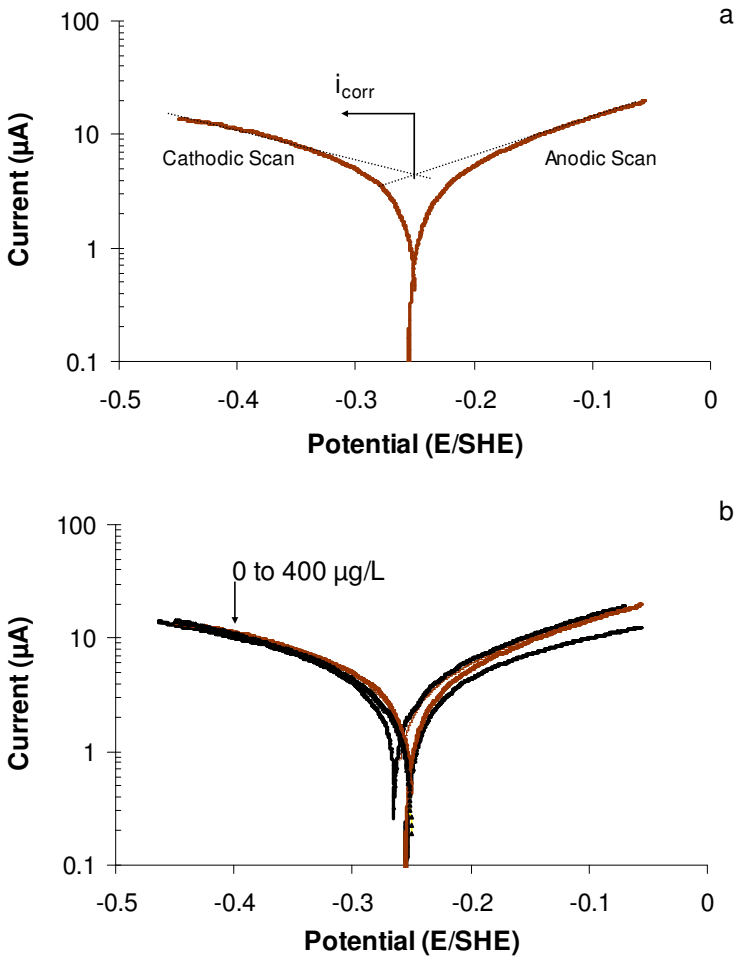

Figure 3.8: a) Tafel scans for the media C graphite paste electrode in Tucson tap water containing no As(V) showing how the corrosion current (i_{corr}) is calculated from extrapolation of the linear regions of the cathodic and anodic scans; b) Tafel scans for the media C graphite paste electrode in Tucson tap water with As(V) concentrations ranging from 0 to 400 µg/L.

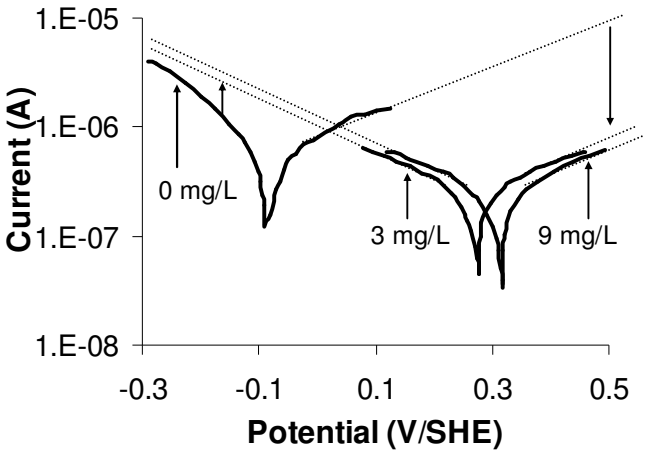

Figure 3.9: Tafel scans for a graphite paste electrode composed of media A at DO concentrations of <0.01, 3 and 9 mg/L.

Table 3.1: Properties of the iron oxide media, iron corrosion products (Fe:As), and hydraulic conductivities of the packed columns, before and after use. Also listed are the changes in DO concentrations (ΔDO), solution pH values (ΔpH), and average effluent iron concentrations for the experiments depicted in Figure 1. The Darcy's law hydraulic conductivity (K) is defined in the supporting information.

Property	Column		
	A	B	AC*
Media composition	100% FeO	60% FeO + 40% Fe_3O_4	75% FeO + 5.3% Fe + 19.5% Fe_2O_3
ΔDO (mg/L)	< 0.1	< 0.1	< 0.3
ΔpH	< 0.3	< 0.3	< 0.3
Effluent Fe (µg/L)	5	5	45
Reaction product Fe:As	15:1	32:1	380:1
Initial K (cm/s)	0.72	0.51	0.20
Final K pre-backwash	0.43	0.48	0.13
Final K post-backwash	0.66	0.51	0.18

*The composition data is for media C. Column AC was packed with 55 g media A and 55 g media C.

CHAPTER 4

UNDERSTANDING REDUCTIVE DECHLORINATION OF TRICHLOROETHENE ON BORON DOPED DIAMOND FILM ELECTRODE

4.1 Abstract

This research investigated reduction of trichloroethylene (TCE) at boron doped diamond film cathodes using a rotating disk electrode reactor. Rates of TCE reduction were determined as a function of the electrode potential and TCE concentration over a temperature range between 12 and 42 °C. TCE reductive dechlorination resulted in the stoichiometric production of acetate with no detectable intermediate products. The rate-limiting step for TCE reduction was dependent on the electrode potential. At potentials more negative than -1.0 V/SHE, the potential dependence of the apparent activation energies for TCE reduction indicated that TCE reduction was not limited by the rate of electron transfer. At potentials less negative than -1.0V/SHE, TCE reaction rates appeared to be limited by an inner sphere electron transfer reaction that involves electron transfer and bond breaking. Density functional simulations indicated that TCE may form a surface complex with oxygen atoms terminating the BDD surface.

4.2 Introduction

In recent years there has been increasing interest in electrochemical methods for removing organic contaminants from water. The main obstacle in developing commercially viable electrochemical water treatment technologies is the need for an electrode material that is stable under anodic polarization. In addition to being stable

when anodically polarized, the material used for the anode in water treatment applications should also be stable when cathodically polarized, because reverse polarization of the electrodes is often required to remove carbonate scale that builds up on the cathodes. Noble metals, such as platinum, are anodically and cathodically stable, but they have high catalytic efficiencies for oxygen evolution and are prone to fouling by chemically adsorbed compounds (81, 82). Dimensionally stable anodes, such as titanium metal coated with active or inactive catalysts, are less prone to oxygen evolution and fouling during anodic polarization, but they do suffer from leaching of the catalyst from the electrode surface under cathodic polarization.

Boron doped diamond film (BDD) electrodes meet the criteria of anodic and cathodic stability required in water treatment applications and have several advantages over other materials, including: 1) high resistance to fouling by chemisorbed metals or other impurities; 2) very low catalytic activity for water electrolysis; 3) high mechanical strength and resistance to chemical attack; 4) high dimensional stability under anodic polarization; and 5) hydrophobicity. Hydrophobic electrodes are desirable for reactions of organic compounds in aqueous systems because of increased organic compound adsorption.

BDD films are most often prepared by chemical vapor deposition (CVD) on p-silicon substrates that have been polished with a diamond containing paste, and thereby contain adsorbed diamond crystals to serve as nucleation sites. Microwave radiation or a hot filament is used to decompose a low pressure (~10 kPa) gas mixture of methane and hydrogen. Upon decomposition, the methyl and atomic hydrogen radicals chemisorb at

the nucleation sites and propagate growth of the film. Boron doping is often accomplished by adding trace amounts of B_2H_6 to the seed gas mixture. The boron atoms substitute for carbon in the diamond lattice at parts per million levels, and serve to increase the electrical conductivity of the diamond film. The resulting films are polycrystalline and may have resistivities as low as < 0.1 Ω-cm (*83*).

Freshly prepared BDD surfaces are terminated with hydrogen atoms (*84*). However, anodic polarization results in oxidation of the surface hydrogen atoms and produces oxygenated functional groups on the BDD surface (*85*). These functional groups are suspected to be involved in mediating electron transfer on BDD electrodes (85, *86*).

BDD electrodes have been extensively studied as anode materials in water treatment applications (*87-90*). However, we are not aware of any published studies of water treatment applications using BDD as a cathode material. The goal of this research was to determine the effectiveness of BDD as cathode for reductive dechlorination of trichloroethylene (TCE). Towards that end, this research investigated the kinetics, reaction mechanisms, reaction products, and Faradaic current efficiencies for TCE destruction by BDD cathodes.

4.3 Electrochemical Kinetics

In the absence of mass transfer limitations, the potential dependence of electrochemical reaction rates can be described by the Butler-Volmer equation (*91*):

$$i = i_0[e^{-\bar{\alpha}F(E-E_{eq})/RT} - e^{\bar{\alpha}F(E-E_{eq})/RT}] \quad (1)$$

where i is net reaction current, i_0 is the exchange current, F is the Faraday constant, R is the gas constant, T is the temperature, E is the electrode potential, E_{eq} is the equilibrium potential for the redox reaction, and $\vec{\alpha}$ and $\bar{\alpha}$ are the electron transfer coefficients for the reduction and oxidation reactions, respectively. The first term in brackets represents the rate of the forward reduction reaction, while the second term gives the rate of the reverse oxidation reaction. The transfer coefficients depend on the number of electrons transferred before ($\vec{\gamma}$) and after ($\bar{\gamma}$) the rate determining step, the number of times the rate determining step must occur, and the symmetry factor (□) for the reaction (*92*). For overall reactions involving only a single TCE molecule, the electron transfer coefficient for reduction may be expressed as:

$$\vec{\alpha} = \vec{\gamma} + r\beta \tag{2}$$

where $r = 0$ if the rate determining step does not involve electron transfer, otherwise $r = 1$. The β parameter is dependent on the symmetry of the potential energy surface between the transition state and the reactant and product species (*92*).

4.4 Materials and Methods

Rotating Disc Electrode (RDE) Experiments**:** Experiments measuring TCE dechlorination rates were performed in a 25 mL temperature controlled glass reaction cell. The working electrode consisted of a boron doped diamond (BDD) film coated on a 1.13 cm diameter p-silicon disk (Adamant Technologies, Neuchatel, Switzerland) contained within a Princeton Applied Research (PAR) (Oak Ridge, TN) model 616 rotating disc electrode holder. To eliminate mass transfer limitations on TCE reaction

rates, the disk electrode was rotated at a speed of 1000 rpm. A 0.3 mm diameter by 4 cm long platinum wire (Aesar, Ward Hill, MA) was used as the counter electrode, and a PAR Hg/Hg_2SO_4 electrode was used as the reference. The counter electrode was encased within a Nafion® (Dupont) proton permeable membrane in order to prevent oxidation of any product or reactant species. Electrode potentials and currents were controlled using a PAR model 273 A potentiostat connected to a PAR model 5210 impedance analyzer. The temperature of the cell was controlled within $\pm 0.2\ ^{\circ}C$ using a circulating water bath.

Experiments measuring TCE dechlorination rates were performed at constant aqueous TCE concentrations in 10 mM $CaSO_4$ background electrolyte solutions with an initial pH value of 7. Constant TCE concentrations were achieved by continuously purging the reaction cell with 25 mL/min of humidified nitrogen gas containing TCE at a fixed concentration. The effect of dissolved oxygen on TCE reaction rates were investigated by purging the reaction cell with 99.99% pure oxygen instead of nitrogen. Apparent activation energies for TCE dechlorination were determined by measuring reaction rates at temperatures ranging from 2 to 42 °C.

Flow Cell Experiments: Because operation of the RDE required that the solution be exposed to the atmosphere through the electrode shaft vent, experiments for determining volatile reaction products were conducted in a Teflon flow-through cell. The previously described BDD disks served as both anode and cathode in the flow cell, and the anode and cathode chambers were separated by a Nafion membrane. Solutions containing TCE

were fed into the cathode compartment and were sampled before entering the anode chamber.

Voltammetry and Impedance Spectroscopy Experiments: Chronoamperometry (CA) and EIS experiments were performed in background electrolyte solutions and in solutions containing TCE. Electrode potentials were controlled and recorded with a PAR model 273A potentiostat and Powersuite software. EIS experiments were conducted by coupling the 273A potentiostat with PAR 5210 impedance phase analyzer. A sinusoidal amplitude modulation of ±10 mV was used over a frequency range from 1 mHz to 100 KHz.

Product Analyses: Rates of TCE dechlorination were determined from the rates of chloride ion generation and the composition of the reaction products. Chloride ion concentrations were determined by triplicate analyses of 5 mL samples using a Dionex DX 500 ion chromatograph and using a chloride ion selective electrode. Reaction products were determined from analyses of aqueous samples using gas chromatography. Chlorinated byproducts were analyzed by extracting 25 µL aqueous samples into 1 g of pentane followed by injection into a Hewlett-Packard (HP) 5890 Series II gas chromatograph (GC) equipped with an electron capture detector (ECD). Nonchlorinated byproducts were analyzed by injecting 10 µL aqueous samples into a modified HP GC equipped with flame ionization detector (FID).

Quantum Mechanical Simulations: Density functional theory (DFT) simulations were performed to determine if TCE can form a chemical adsorption complex on BDD surfaces. Unrestricted spin DFT calculations were performed using the DMol^3 (*93*) package in the Accelrys Materials Studio modeling suite (*94*) using a personal computer operating with a 2.8 GHz Pentium 4 processor. All simulations used double-numeric with polarization (DNP) basis sets (*93*, *95*) and the gradient corrected Vosko-Wilk-Nusair and Becke-Perdew (VWN-BP) functionals for correlation and exchange.

Simulations were performed on both completely hydrogen terminated and oxygen modified diamond clusters containing 10 carbon atoms. FTIR analyses indicated that the diamond surface contained carbonyl functional groups. Therefore, oxygen was incorporated in the diamond surfaces in the form of carbonyl groups on the [100] face of the diamond crystal.

4.5 Results and Discussion

Reduction of TCE resulted in near stoichiometric production of acetate, which accounted for 94 to 102% of the TCE mass balance. TCE reduction was accompanied by a decline in solution pH values, with an average of 4 moles of H^+ produced per mole of TCE reduction. The overall stoichiometry for this reaction can be described by:

$$\text{cathode reaction}: \ CHClCCl_2 + 2H_2O + 2e^- \rightarrow CH_3COO^- + 2\ H^+ + 3\ Cl^- \qquad (3)$$

$$\text{anode reaction}: \ H_2O \rightarrow 0.5\ O_2 + 2\ e^- + 2\ H^+ \qquad (4)$$

The absence of any intermediate chlorinated products suggests that TCE reduction occurs via an inner sphere electron transfer mechanism that may involve chemisorbed

intermediates. Reactions involving a chemically adsorbed surface complex may explain why TCE reduction on BDD surfaces produce acetate, whereas TCE reduction at metal electrodes produces ethene and ethane.

The potential dependence of TCE reduction rates can be used to determine the electron transfer coefficient for TCE reduction, as illustrated in Figure 4.1a. Reaction kinetics conforming to the Butler-Volmer equation should be characterized by a single $\bar{\alpha}$ value. The data in Figure 4.1a indicates that there are two electron transfer coefficients for TCE reduction. At potentials between -0.5 and -1.5 V/SHE, α=0.099±0.005, while at more negative potentials α=0.006±0.002. The decrease in $\bar{\alpha}$ values with decreasing potentials suggests that there is a change in the rate-limiting step. With decreasing potentials, rates of electron transfer should increase exponentially, while rates of chemical dependent steps, such as, adsorption of the reactant, bond breaking, atomic rearrangement, or desorption of the product species, should show little or no potential dependence. Therefore, the decrease in slope at potentials more negative than -1V/SHE suggests that a chemical dependent step limits TCE reaction rates in this potential range.

The temperature dependence of TCE reaction rates at potentials between -1.25 and -3.75 V/SHE indicate that TCE reduction was not limited by an electron transfer step at potentials more negative than -1.25 V/SHE. TCE reaction rates measured at 12, 22, 32 and 42 °C were used to determine apparent activation energies for TCE reduction, as illustrated in Figure 4.2a. The dependence of the apparent activation energies as a function of the electrode potential are shown in Figure 4.2b. According to the Butler-

Volmer equation, the apparent activation energies should decline with electrode potential, according to (92):

$$E_a = E_a^{eq} + \bar{\alpha}F(E - E_{eq}) \quad (5)$$

where E_a^{eq} is the activation energy at the equilibrium potential. For TCE reduction, cathodic polarizations resulted in negative overpotentials (E-E_{eq}). Therefore, if TCE reduction was limited by an electron transfer step, decreasing E_a values with increasingly negative electrode potentials should have been observed. The data in Figure 4.2b show that E_a actually increases with increasing overpotentials, thus indicating that TCE reduction was not limited by rates of electron transfer.

At potentials less negative than -1.0V/SHE the small value of $\bar{\alpha}$ also suggests that the rate of electron transfer was not the only factor limiting the rate of TCE reduction. According to equation 2, electron transfer coefficients <1 indicate that zero electrons are transferred before the rate-limiting step. Therefore, if the rate-limiting step involves the transfer of the first electron (*i.e.*, r = 1 in eqn. 2), $\bar{\alpha} = \beta$. The $\bar{\alpha}$ of 0.10 observed at potentials less negative than -1.0 V/SHE in Figure 4.1a is well-below the range of β values of close to 0.5 that are normally observed for reactions that are limited by outer-sphere electron transfer (92). This suggests that the rate of TCE reduction at potentials less negative than -1.0 V/SHE was limited by an inner sphere electron transfer step, such as a concerted electron transfer and bond breaking step.

Density functional simulations were used to investigate possible TCE reaction mechanisms at the BDD surface. For uncharged systems, there was no reaction between TCE and either the H- or O-terminated diamond surface. However, simulations with a negative charge on the cluster, as would be the case for a diamond cathode, resulted in the formation of a chemisorption complex between TCE and the diamond surface. Figure 4.3a shows the initial starting configuration for a diamond cluster with a net charge of -1 and Figure 4.3b shows the resulting chemisorption complex. Complex formation of TCE with the diamond surface resulted in the loss of one chloride ion and the formation of a bond between one carbon atom in TCE and the oxygen atom on the diamond surface. The formation of a chemisorbed intermediate may explain the absence of dichlorinated reaction products in the solution. Formation of a chemical bond between the TCE residue and the surface likely enables a sufficiently long surface interaction that allows complete dechlorination before desorption of the product species back into solution.

EIS was used to detect the presence of a surface adsorbed intermediate on the electrode surface. Figure 4.4 shows the phase angle between the applied potential and the resulting current in blank electrolyte and TCE containing solutions during an EIS scan. The negative phase angle at frequencies below 0.05 Hz in the TCE solution indicates the presence of inductance. Inductance at low frequencies is normally associated with a slow surface reaction that limits the rate of electron transfer. This slow surface reaction could be associated with a chemisorbed intermediate on the electrode surface.

4.6 Competing Reactions

The effect of reactive site saturation and reactant product inhibition on rates of TCE reduction were investigated by varying the TCE and reaction product concentrations. The effect of TCE concentration on its reaction rate was typical of that observed for site limited surface reactions. At TCE concentrations below 1 mM, TCE reaction rates were approximately first order in TCE concentration, whereas with increasing concentration, reaction rates approached zeroth order in TCE concentration.

There was inhibition of TCE reaction rates by the reaction product, acetate. Experiments investigating the effect of acetate on TCE reaction rates at a fixed TCE concentration of 7.5 mM indicated that there was a near linear decline in the TCE reaction rate with increasing acetate concentration, as shown in Figure 4.5. This inhibitory effect of acetate on TCE reaction rates suggests that desorption rates of the reaction product may limit TCE reduction rates. However, under most experimental conditions, the maximum acetate concentration in experiments with no added acetate was 0.180 mM. Therefore, the effect of the solution phase acetate concentration on the measured TCE rates was negligible and was less than the experimental error.

Hydrogen evolution was the main reaction competing with TCE reduction on the electrode surface. Figure 4.6a shows the Faradic current efficiency for TCE reduction as a function of the current density for TCE concentrations of 0.375, 3 and 7.5 mM. For all TCE concentrations, the Faradic efficiency declines with increasing current density. This results from the electron transfer coefficient for hydrogen evolution being greater than that for TCE reduction. Also shown in Figure 4.6a is the Faradic current efficiency for TCE reduction by an iron disk electrode determined in a previous investigation (*96*). On

the BDD surface, the current efficiencies appear to be approximately two times greater than those on iron. The current efficiencies are greater on BDD despite TCE reduction on BDD being a 2 electron reduction whereas TCE reduction on iron is a 6 electron reduction (96). In addition to showing higher Faradic current efficiencies than zerovalent iron, the reaction rates for TCE reduction on BDD electrodes are faster than on zerovalent iron. The combination of faster rate and higher current efficiency leads to about a one order of magnitude greater reduction rate at comparable current efficiencies, as shown in Figure 4.6b.

This research shows that TCE reduction at BDD cathodes occurs via a mechanism that appears to involve chemically adsorbed intermediate species. This may explain why the reaction products for TCE reduction on BDD electrodes are considerably different than those on metal electrodes. Current efficiencies and reaction rates for TCE reduction on BDD electrodes are greater than those on iron cathodes at comparable current densities.

4.7 Acknowledgements

Acknowledgement is made to the donors of The American Chemical Society Petroleum Research Fund for support of this research.

4.8 Figures

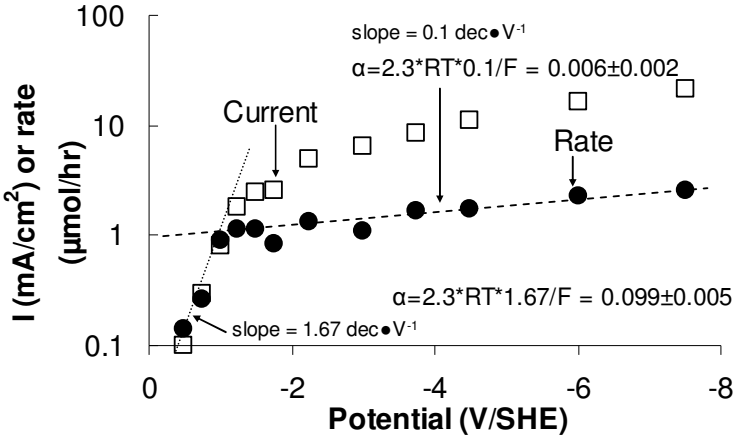

\

Figure 4.1: a) Rate of TCE reduction (●)in µmol● hr^{-1} or current density (□) in mA●cm^{-2} on BDD surface at different electrode potential (V/SHE) for 7.5 mM TCE at 22 ^{0}C.

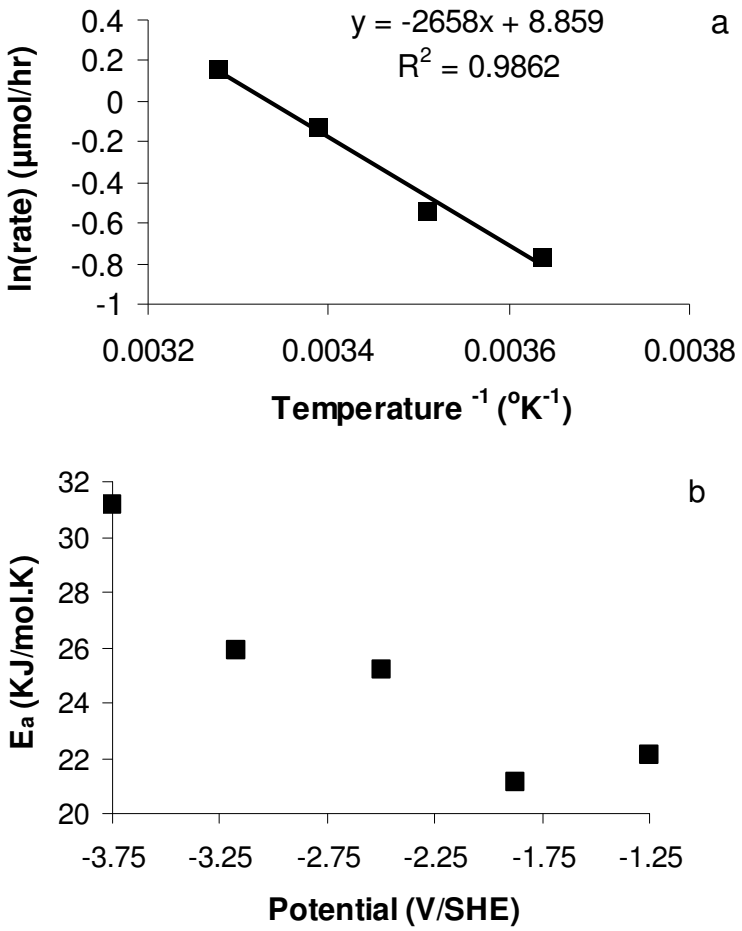

Figure 4.2: a) TCE reduction rate in µmol● hr^{-1} versus inverse of reaction temperature (T^{-1}) at a fixed TCE concentration of 3.0 mM. b) Activation energies (kJ●mol^{-1}) as a function of electrode potential (V/SHE) calculated from part a.

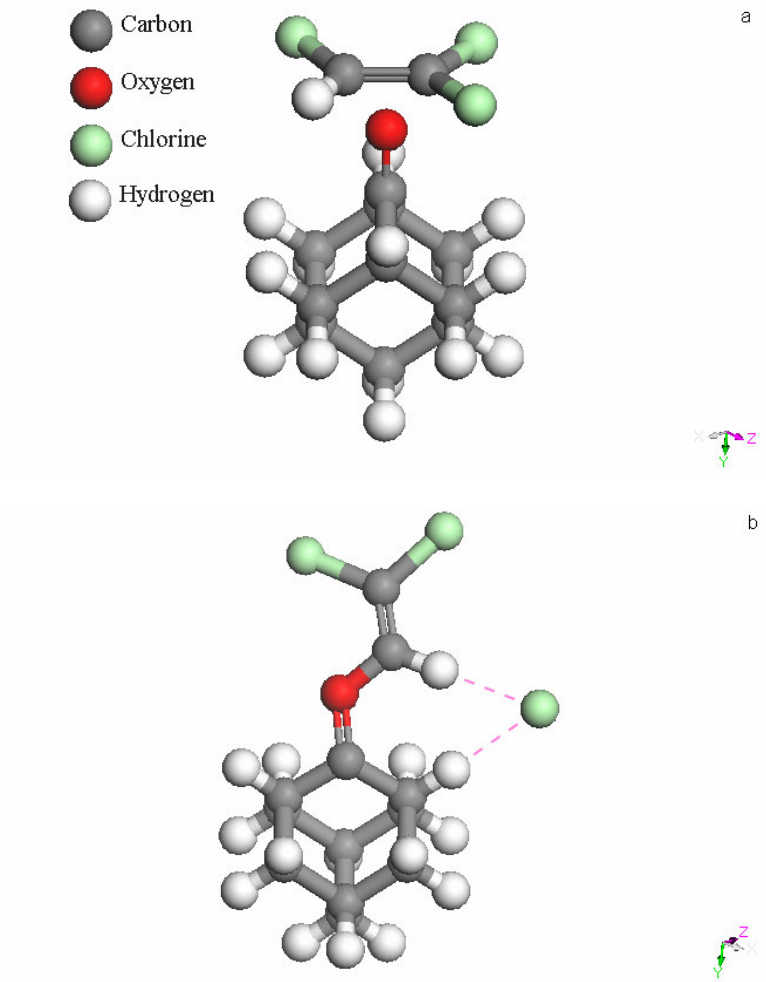

Figure 4.3: a) Density functional theory simulation for the initial starting configuration for a diamond cluster with net charge of -1. b) Resulting chemisorbed complex for part a).

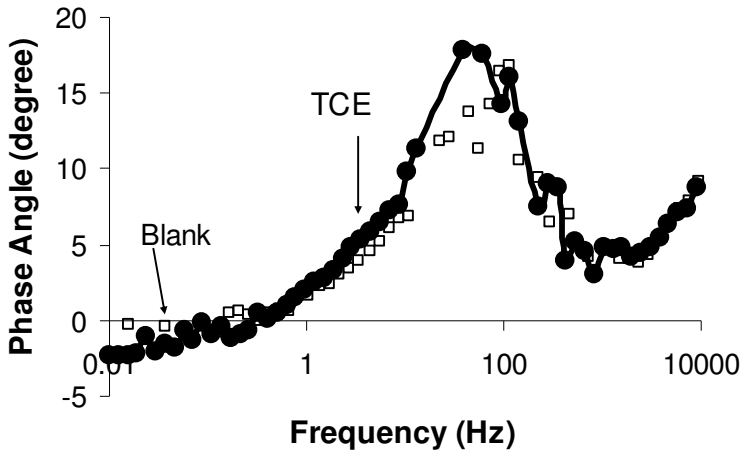

Figure 4.4: Bode Phase plots of the phase angle between the applied voltage and resulting currents as a function of the signal frequency at 0 mM (□) and 7.5 mM (●)TCE concentration.

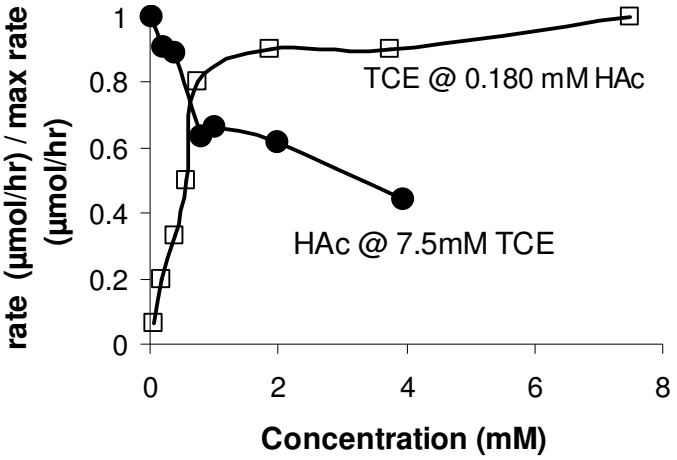

Figure 4.5: TCE reduction rate (□) in µmol● hr^{-1} on BDD surface as a function of the aqueous TCE concentration in mM at 22 ^{0}C and 15 mA●cm^{-2} and HAc (●) concentration (mM).

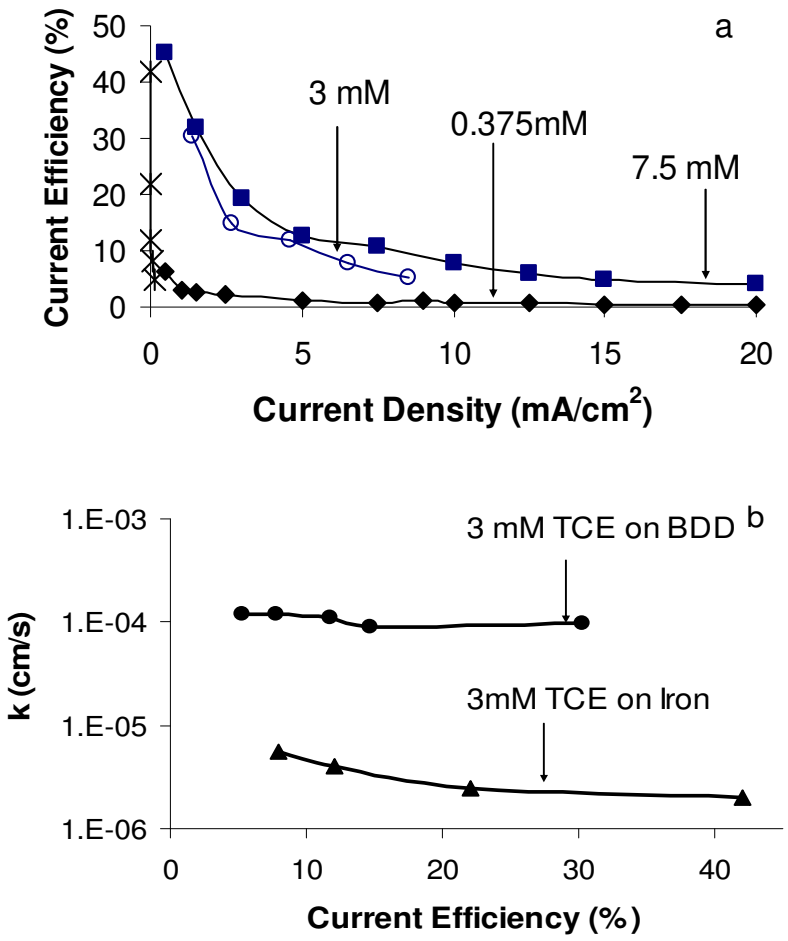

Figure 4.6: a) Current efficiency (%) as a function of current density (mA●cm^{-2}) for 0.375 (♦), 3.0 (○), 7.5 mM (■) TCE on BDD surface and 3.0 mM (X) TCE on iron surface. b) Surface area normalized rate constants k (cm/s) as a function of the current efficiency for BDD and iron electrodes.

REFERENCES

1 O'Hannesin, S. F.; Gillham, R. W. Long-term performance of an in situ "iron wall" for remediation of VOCs. *Groundwater* **1998**, *36*, 164.

2 Yabusaki, S.; Cantrell, K.; Sass, B.; Steefel, C. Multicomponent reactive transport in an in situ zero-valent iron cell. *Environ. Sci.Technol.* **2001**, *35*, 1493.

3 Vogan, J. L.; Focht, R. M.; Clark, D. K.; Graham, S. L. Performance evaluation of a permeable reactive barrier for remediation of dissolved chlorinated solvents in groundwater. *J. Hazard. Mater.* **1999**, *68*, 97.

4 McMohan, P. B.; Dennehy, K. F.; Sandstorm, M. W. Hydraulic and geochemical performance of a permeable reactive barrier containing zero-valent iron, Denver Federal Center. G*roundwater* **1999**, *37*, 396.

5 Gilham, R. W.; O'Hannesin, S. F. Enhanced degradation of halogenated aliphatics by zero-valent iron. *Groundwater* **1994**, *32*, 958.

6 Peterson, M. L.; White, A. F.; Brown, G. E., Jr.; Parks, G. Surface Passivation of Magnetite by Reaction with Aqueous Cr(VI): XAFS and TEM Results. *Environ. Sci. Technol.* **1997**, 31, 1573.

7 Williams, A. G.; Scherer, M. M. Kinetics of Cr(VI) reduction by carbonate green rust. E*nviron. Sci. Technol*. **2001**, 35, 3488.

8 Dixit, S.; Hering, J. G. Comparison of Arsenic(V) and Arsenic(III) Sorption onto Iron Oxide Minerals: Implications for Arsenic Mobility. *Environ. Sci. Technol*. **2003**, 37, 4182.

9 Gu, B.; Watson, D. B.; Wu, L.; Phillips, D. H.; White, D. C.; Zhou, J. Microbiological characteristics in a zero-valent iron reactive barrier. *J. Environ. Monit. Assess*. **2002**, 77, 293.

10 Till, B. A.; Weathers, L. J. Fe(0)-Supported Autotrophic Denitrification. *Environ. Sci. Technol.* **1998**, *32*, 634.

11 Rahman, A.; Agrawal, A. Reduction of nitrate and nitrite by iron metal: Implications for ground water remediation. Book of Abstracts, 213th ACS National Meeting, April 13-17, **1997**, San Francisco, CA.

12 Alowitz, M. J.; Scherer, M. Kinetics of nitrate, nitrite, and Cr(VI) reduction by iron metal. *Environ. Sci. Technol.* **2002**, *36*, 299.

13 Cheng, I. F.; Muftikian, R.; Fernando, Q.; Korte, N. Reduction of nitrate to ammonia by zero- valent iron. *Chemosphere* **1997**, *35*, 2689.

14 Westerhoff, P.; James, J. Nitrate removal in zero-valent iron packed columns. Water Research, **2003**, 37, 1818.

15 Schlicker, O.; Ebert, M.; Fruth, M.; Weidner, M.; Wust, W.; Dahmke, A. Degradation of TCE with iron: the role of competing chromate and nitrate reduction. *Groundwater* **2000**, *38*, 403.

16 Farrell, J.; Kason, M.; Melitas, N. T.; Li, T. Electrochemical and Column Investigation of Iron-Mediated Reductive Dechlorination of Trichloroethylene and Perchloroethylene. *Environ.Sci. Technol.* **2000**, *34*, 514.

17 Chew, F. F.; Zhang, T. C. *Environ. Sci. Technol.* **1999**, *16*, 389.

18 Choe, S.; Chang, Y.; Hwang K. Y.; Khim, J. *Chemosphere* **2000,** 41, 1307.

19 Huang, C. P.; Wang, H. W.; Chiu, P. C. *Water Res.* **1998**, *32*, 2257

20 Shanshan, J.; Pei, C. *Abstract of Papers*, 31 *st* Mid-Atlantic Industrial and Hazardous Waste Conference ,Atlanta,**1999**; 240.

21 Ritter, K.; Odziemkowski, M. S.; Simpgraga, R.; Gillham, R. W.; Irish, D. E. *J. Contaminant Hydrology* **2003**, *65*, 121.

22 Siantar, D. P.; Schrier, C. G.; Chou, C. S.; Reinhard, M. *Water Res.* **1996**, *30*, 2315

23 American Public Health Association; American Water Works Association; Water Environment Fedration, *Standard Method for the Examination of Water and Waste Water*; 19th ed., **1995.**

24 Uhlig, H. H.; Revie, R. W. *Corrosion and Corrosion Control*; 3rd ed.; John Wiley: New York, **1985.**

25 Ma, H.; Cheng, X.; Li, G.; Chen, S.; Quan, Z.; Zhao, S.; Niu, L. *Corros. Sci.* **2000**, *42*, 1669.

26 Benedetti, A. V.; Sumodjo, P. T. A.; Nobe, K.; Cabot, P. L.; Proud, W. G. *Electrochim. Acta* **1995**, *40*, 2657.

27 Tait, S. W. *An Introduction to Electrochemical Corrosion Testing for Practice Engineers and Scientists*; Pair O Docs Publications: Racine, WI, **1994**.

28 Bockris, J. O. M.; Reddy, A. K. N. *Modern Electrochemistry*; Plenum Press: New York, **1970**.

29 Melitas, N.; Farrell, J.; Chuffe-Moscoso, O. *Environ. Sci. Technol.* **2001**, *35*, 3948

30 Brown, A. P.; Krumpelt, R. O.; Yao, N. P. *J. Electrochem. Soc.* **1982**, *129*, 2481.

31 Cornell, A.; Lindbergh, G.; Simonsson, D. *Electrochim. Acta* **1992**, *37*, 1873.

32 Kreysa, G.; Haakansson, B. *J. Electroanal. Chem.* **1986**, *201*, 61.

33 Stumm, W. *Chemistry of the Solid Water Interface: Processes at the Mineral-Water and Particle-Water Interface of Natural Systems*; Wiley: New York, **1992**.

34 Pourbaix, M. *Atlas of Electrochemical Equilibria;* Pergamon Press: Oxford*,* **1966**.

35 Cornell, R. M.; Schwertmann, U. *The Iron Oxides*; 3rd ed.; VCH Publishers, New York, **1996**.

36 Pierce, M. L.; Moore, C. B. Adsorption of arsenite and arsenate on amorphous iron hydroxide. *Wat. Res.* **1982**, 16, 1247-1253.

37 Goldberg, S. Chemical modeling of arsenate adsorption on aluminum and iron oxide minerals. *Soil Sci. Soc. Am. J.* **1986**, 5, 1154-1157.

38 Waychunas, G. A.; Rea, B. A.; Fuller, C. C.; Davis, J. A. Surface chemistry of ferrihydrite: Part 1: EXAFS studies of the geometry of coprecipitated and adsorbed arsenate. *Geochim. Cosmochim. Acta*. **1993**, 57, 2251-2269.

39 Fuller, C. C.; Davis, J. A.; Waychunas, G. A. Surface chemistry of ferrihydrite: Part 2: Kinetics of arsenate adsorption and coprecipitation. *Geochim. Cosmochim. Acta*. **1993**, 57, 2271-2282.

40 Fendorf, S.; Eick, M. J.; Grossl, P. Sparks, D. L. Arsenate and chromate retention mechanisms on goethite. 1: Surface structure. *Environ. Sci. Technol.* **1997**, 31, 315-320.

41 Grossl, P. R.; Eick, M.; Sparks, D. L.; Goldberg, S.; Ainsworth, C. C. Arsenate and chromate retention mechanisms on goethite. 2: Kinetic evaluation using a pressure-jump relaxation technique. *Environ. Sci. Technol*. **1997**, 31, 321-326.

42 Raven, K. P.; Jain, A.; Loeppert, R. H. Arsenite and arsenate adsorption on ferrihydrite: Kinetics, equilibrium, and adsorption envelopes. *Environ. Sci. Technol.* **1998**, 32, 344-349.

43 Manning, B. A.; Fendorf, S. E.; Goldberg, S. Surface structures and stability of arsenic(III) on goethite: Spectroscopic evidence for inner-sphere complexes. *Environ. Sci. Technol.* **1998**, 32, 2383-2388.

44 Jain, A.; Raven, K. P. Loeppert, R. H. Arsenite and arsenate adsorption on ferrihydrite: Surface charge reduction and net OH^- release stoichiometry. *Environ. Sci, Technol.* **1999**, 33, 1179-1184.

45 Haron, M. J.; Wan Yunus, W. M. Z.; Yong, N. L.; Tokunaga, S. Sorption of arsenate and arsenite anions by iron(III)-poly(hydroxamic acid) complex. *Chemosphere*, **1999**, 39, 2459-2466.

46 Su, C.; Puls, R. W. Significance of iron (II,III) hydroxycarbonate green rust in arsenic remediation using zerovalent iron in laboratory column tests. *Environ. Sci. Technol.* **2004**, 38, 5224-5231.

47 Su, C.; Puls, R. W. Arsenate and arsenite removal by zerovalent iron: Kinetics, redox transformation, and implications for in situ groundwater remediation. *Environ. Sci. Technol.* **2001**, 37, 1487-1492.

48 Lackovic, J. A.; Nikolaidis, N. P.; Dobbs, G. M. Inorganic arsenic removal by zero-valent iron. *Environ. Sci. Technol.* **2000**, 17, 29-39.

49 Bang, S.; Korfiatis, G. P.; Meng, X. Removal of arsenic from water by zerovalent-iron. *J. Hazardous Materials*, **2005**, 121, 67-67.

50 Bang, S.; Johnson, M. D.; Korfiatis, G. P.; Meng, X. Chemical reactions between arsenic and zero-valent iron in water. *Wat. Res.* **2005**, 39, 763-770.

51 Driehaus, W.; Jekel, M.; Hildebrandt, U. Granular Ferric Hydroxide – A New adsorbent for the removal of arsenic from natural water. *J. Water SRT- Aqua*, **1998**, 47, 1, 30-35.

52 Jing, C.; Liu, S.; Patel, M.; Meng, X. Arsenic leachability in water treatment adsorbents. *Environ. Sci. Technol*. **2005**, 39, 5481-5487.

53 Cheng, Z.; Nikolaidis, N. P.; Van Geen, A.; Bailey, R. C.; Westgate, M. Arsenic removal by zero-valent iron: Field tests in rural Bangladesh and at the Vineland Chemical, NJ, Superfund site. *Abstract of papers, 226th ACS national meeting*, **2003**, New York, NY.

54 Alauddin, M.; Hussam, A.; Khan, A. H.; Habibuddowla, M.; Rasul, S. B.; Munir, A. K. M. Critical evaluation of a simple arsenic removal method for groundwater of Bangladesh. *Proceedings of 4th international conference on arsenic exposure and health effects*, **2000**, San Diego, CA.

55 Petrusevski, B.; Sharma, S. K.; Kruis, F.; Omeruglu, P.; Schippers, J. C. Family filter with iron-coated sand: Solution for arsenic removal in rural area. *Water Sci. Technol: Wat. Supply,* **2002**, 2, 127-133.

56 Nikolaidis, N. P.; Dobbs, G. M.; Lackovic, J. A. Arsenic removal by zerovalent-iron: Field, laboratory and modeling studies. *Wat. Res*. **2003**, 37, 1417-1425.

57 Farrell, J.; Wang, J.; O'Day, P.; Conklin, M. Electrochemical and spectroscopic study of arsenate removal from water using zerovalent iron media. *Environ. Sci. Technol.* **2001** 35, 2026-2032.

58 Sepulveda, R. *Master's Thesis*, University of Arizona, **2002**.

59 Westerhoff, P.; Highfield, D.; Badruzzaman, M.; Yoon, Y. Rapid small-scale column test for arsenate removal in iron oxide packed bed columns. *J. Environ. Eng*. **2005**, 131, 262-271.

60 Badruzzaman, M.; Westerhoff, P.; Knappe, D. R. U. Intraparticle diffusion and adsorption of arsenate onto granular ferric hydroxide. *Wat. Res.* **2004**, 38, 4002-4012.

61 Melitas, N.; Wang, J.; Conklin M.; O'Day, P.; Farrell, J. Understanding soluble arsenate removal kinetics by zerovalent iron media. *Environ. Sci. Technol*. **2002**, 36, 2074-2081.

62 USEPA, Method 9100: Saturated hydraulic conductivity, saturated leachate conductivity, and intrinsic permeability. EPA SW-846, **1986**, Washington, DC.

63 Bear, J. *Hydraulics of Groundwater*, McGraw-Hill, New York, **1979**.

64 USEPA, Method 6020A: Inductive coupled plasma-mass spectrometry. EPA SW-846, **1998**, Washington, DC.

65 USEPA, Method 0370.1: Silica, dissolved -colorimetric. EPA 600/4-79-020, **2003**, Washington, DC.

66 Jeon, B. H.; Dempsey, B. A.; Burgos, W. D. Kinetics and mechanisms for reactions of Fe(II) with iron(III) oxides. *Environ. Sci. Technol.* **2003**, 37, 3309-3315.

67 Zheng, Y.; Stute. M.; Van Geen, A.; Gavrieli, I.; Dhar, R.; Simpson, H.; Schlosser, P.; Ahmed, K. M. Redox control of arsenic mobilization in Bangladesh groundwater. *Applied Geochem*. **2004**, 19, 201-214.

68 Su, C.; Puls, R. W. Arsenate and Arsenite Removal by Zerovalent Iron: Effects of phosphate, silicate, carbonate, borate, sulfate, chromate, molybdate, and nitrate, relative to chloride. *Environ. Sci. Technol*. **2001**, 35, 4562-4568.

69 Meng, X.; Korfiatis, G. P.; Bang, S.; Bang, K. W. Combined effects of anions on arsenic removal by iron hydroxides. *Toxicology Letters.* **2002**, 133, 103-111.

70 Su, C.; Puls, R. W. In situ remediation of arsenic in simulated groundwater using zerovalent iron: Laboratory column tests on combined effects of phosphate and silica. *Environ. Sci. Technol.* **2003**, 37, 2582-2587.

71 Cheng, Z.; Van Geen, A.; Jing, C.; Meng, X.; Seddique, A.; Amed, K. M. Performance of a household-level arsenic removal system during 4-month deployments in Bangladesh. *Environ. Sci. Technol*. **2004**, 38, 12, 3442-3448.

72 Meng, X.; Bang, S.; Korfiatis, G. P. Effects of silicate, sulfate and carbonate on arsenic removal by ferric chloride. *Wat. Res*. **2000**, 34, 1255-1261.

73 Davis, C. C.; Knocke, W. R.; Edwards, M. Implications of aqueous silica sorption to iron hydroxide: Mobilization of iron colloids and interference with sorption of arsenate and humic substances. *Environ. Sci. Technol*. **2001**, 35, 3158-3162.

74 Wilson, E. J.; Geankoplis, C. J. Liquid mass transfer at very low Reynolds numbers in packed beds. *Ind. Eng. Chem. Fundam.* **1966***,* **5**, 9-14.

75 Park, B.; Dempsey, B. A. Heterogeneous oxidation of Fe(II) on ferric hydroxide at neutral pH and a low partial pressure of O_2. *Environ. Sci. Technol*. **2005**, 39, in press.

76 Dixit, S.; Hering, J. G. Comparison of arsenic(V) and arsenic(III) sorption onto iron oxide minerals: Implications for arsenic mobility. *Environ. Sci. Technol.* **2003**, 37, 4182-4189.

77 Daus, B.; Weib, H.; Wennrich, R. Arsenic speciation in iron hydroxide precipitates. *Talant*a **1998**, 46, 867-873.

78 Ford, R. Rates of hydrous ferric oxide crystallization and the influence on coprecipitated arsenate. *Environ. Sci. Technol*. **2002**, 36, 24 9-2463.

79 Uhlig, H. H.; Revie, R. W. *Corrosion and Corrosion Control*. 3rd ed.; John Wiley: New York, **1985**.

80 Bear, J. *Hydraulics of Groundwater*, McGraw-Hill, New York, **1979**.

81 Gyorgy, F.; Gandini, D.; Comninellis, C.; Perret, A.; Haenni, W. Oxidation of organics by intermediates of water discharge on IrO_2 and synthetic diamond anodes. *Electrochemical and Solid State Letters* **1999**, 2, 228-230.

82 Comninellis, Ch.; Nerini, A. Anodic oxidation of phenol in the presence of NaCl for wastewater treatment. *J. Appl. Electrochem*. **1995**, *25*, 23-29.

83 Xu, J.; Granger, M. C.; Chen, Q.; Strojek, J. W.; Lister, T. E.; Swain, G. M. Boron-doped diamond thin-film electrodes. *Analytical Chem*. **1997**, 69, 591A-597.

84 Martin, H.; Argoitia, A.; Landau, U.; Anderson, A. B.; Angus, J. C. Hydrogen and oxygen evolution on boron-doped diamond electrodes. *J. Electrochem. Soc*. **1996**, 143, L133-L136.

85 Latto, M. N.; Riley, D. J.; May, P. W. Impedance studies of boron-doped CVD diamond electrodes. *Diamond and Related Materials,* **2000**, 9, 1181-1183.

86 Martin, H.; Argoitia, A.; Landau, U.; Anderson, A. B.; Angus, J. C. Hydrogen and oxygen evolution on boron-doped diamond electrodes. *J. Electrochem. Soc*. **1996**, 143, (6), L133-L136.

87 Gyorgy, F.; Gandini, D.; Comninellis, C.; Perret, A.; Haenni, W. Oxidation of organics by intermediate of water discharge on IrO_2 and synthetic diamond anode. *Electrochemical and Solid State Letters*, **1999**, 2, 228-230.

88 Gherardini, L.; Michaud, P. A.; Panizza, M.; Comninellis, Ch. Electrochemical oxidation of 4-chlorophenol for wastewater treatment. *J. Electrochem. Soc*. **2001**, 148, D78-D82.

89 Hagans, P. L.; Natishan, P. M.; Stoner, B. R.; O'Grady, W. E. Electrochemical oxidation of phenol using boron-doped diamond electrodes. *J. Electrochem. Soc*. **2001**, 148, E298-E301

90 Iniesta, J.; Michaud, P. A.; Panizza, M.; Cerisola, G.; Aldaz, A.; Comninellis, Ch. Electrochemical oxidation of phenol at boron-doped diamond film electrode. *Electrochimica Acta*. **2001**, 46, 3573-3578.

91 Bard, A. J.; Faulkner, L. R. *Electrochemical Methods;* John Wiley and Sons: New York, **1980**.

92 Bockris, J. O'M.; Reddy, A. K. *Modern Electrochemistry, Volume 2*; Plenum Press: New York, **1970**.

93 Delley, B. An all-electron numerical-method for solving the local density functional for polyatomic-molecules. *J. Chem. Phys.* **1990**, 92, 1, 508-517.

94 Accelrys, Inc. Material Studio 2.2; San Diego, CA, **2001**.

95 Delley, B. Fast calculation of electrostatics in crystals and large molecules. *J. Phys. Chem.* **1996**, 100, 15, 6107-6110.

---

96 Li, T.; Farrell, J. Electrochemical Investigation of the Rate-Limiting Mechanisms for Trichloroethylene and Carbon Tetrachloride Reduction at Iron Surfaces, *Environ. Sci. Technol.* **2001**,35, 3560-3565.